Thermal performance of an ice storage device for cooling compressed mine air in high-temperature mine refuge chambers

Zujing Zhang[a,b*], Weishuang Guo[a], Hongwei Wu[c], Liang Ge[b], Xing Liang[d], Ruiyong Mao[a**]

[a] College of Civil Engineering, Guizhou Provincial Key Laboratory of Rock and Soil Mechanics and Engineering Safety, Guizhou University, Guiyang, 550025, China.

[b] State Key Laboratory of Gas Disaster Detecting, Preventing and Emergency Controlling, Chongqing Research Institute of China coal Technology and Engineering Group Co. Ltd, Chongqing, 400037, China.

[c] School of Physic, Engineering and computer science, University of Hertfordshire, Hatfield, AL10 9AB, United Kingdom.

[d] School of Computer Science and Mathematics, Kingston University London, KT1 2EE, United Kingdom

[*]Corresponding author: tel: +86 185 2391 9513 email: zjzhang3@gzu.edu.cn.

[**]Corresponding author: tel: +86 139 8505 6628 email: rymao@gzu.edu.cn.

Abstract: Power outages and the risk of explosion in disaster areas make the temperature control in hot mine refuge chambers become extremely challenging. In this article, an ice storage cooling mine compressed air device with a volume of 1 m^3 was newly developed for high-temperature mine refuge chambers. Both the ice storage performance and the compressed air cooling performance of the device were tested in a systematic manner. A full-size numerical model was established and validated against experimental data. The effects of the heat exchange tubes number, inlet air velocity and inlet air temperature on its thermal performance were analyzed in detail. Results indicate that: (i) the ice storage function is completed within 60 h with the ice being cooled to below -15℃. (ii) When the number of heat exchange tubes is 18, the device achieves the best thermal performance with an ice melting rate of 85.02% within 96 h, and the average outlet temperature could be cooled to approximately 20℃. (iii) increasing the inlet air temperature from 30 to 34℃ could increase the ice melting rate by 4.59%, and increasing the inlet air velocity from 5 to 15 m/s could increase the ice melting rate by 16.36%. the rational allocation of cold storage capacity by mixing air supply is the key to improving the utilization rate of the cold capacity and prolonging the effective temperature control time of the refuge chamber.

Keywords: Mine refuge chamber; Ice storage cooling device; Mine compressed air; Phase change energy storage technology; Energy distribution.

Nomenclature			
A	Heat transfer area, m^2	*Subscripts*	
c_a	Specific heat capacity of air, kJ/(kg · K)	h_{ref}	Reference surface enthalpy, kJ/kg
c_i	Specific heat capacity of ice, kJ/(kg·℃)	h_{sens}	Material sensible enthalpy, kJ/kg
c_w	Specific heat capacity of water, kJ/(kg · K)	h_1	Cold air enthalpy, kJ/kg
C_m	Mushy zone constant, kg/(m3·s)	h_2	Hot air enthalpy, kJ/kg
C_1,C_2,C_3	Model parameters	T_v	Ventilation temperature, ℃
d	Tube diameter, mm	T_{ref}	Reference surface temperature, ℃
E	Enthalpy of the phase transition, kJ/kg	i	Vector direction
g	gravity acceleration, m/s^2	j	Vector direction
k	Heat transfer coefficient, $W/(m^2 \cdot K)$	q_1	Cold air mass flow rate, kg/h
L	Tube length, m	q_2	Hot air mass flow rate, kg/h
M	Air mass flow rate, kg/s	q_r	Per capita heat dissipation power, J/s
N	Number of tubes	r_i	Latent heat of ice melting, J/kg
p	Pressure, Pa	t_w	Temperature of the pipe wall, ℃
Q_i	Cold storage capacity, kJ	T_v	Ventilation temperature, ℃
Q_r	The total heat load of MRC, kJ	T_{solid}	Water solidification temperature, ℃
V	Amount of ice storage, m^3	T_{liquid}	Water melting temperature, ℃
Dimensionless		u_1	Directly uncertain reading
Nu	Nusselt number	U_2	Indirect uncertain reading
Pr	Prandtl number	*Acronyms*	
Re	Reynolds number	ADV	Air delivery volume
Greek symbols		AOT	Average outlet temperature
α	Coefficient of thermal expansion, 1/K	CTD	Cooling temperature difference
γ	Liquid volume fraction	HETN	Heat exchange tubes' number
ε	Turbulent energy dissipation, J/(kg · s)	IAT	Inlet air temperature
κ	Turbulent kinetic energy, (J/kg)	IAV	Inlet air velocity
λ	Thermal conductivity, W/(m · K)	IMR	Ice melting rate
μ	Dynamic viscosity coefficient, $N \cdot s/m^2$	ISCMCAD	Ice storage cooling mine compressed air device
ν	Motion viscosity coefficient, m^2/s	ISRT	Initial surrounding rock temperature
ξ	Constant,9.3×10^{-6}	MCA	Mine compressed air
ρ	Density, kg/m^3	MRC	Mine refuge chamber
τ	Time, h	OAT	Outlet air temperature
ω	Constant, 0.0001		

1. Introduction

Energy is an important material foundation for social development, which directly affects socio-economic security and sustainable development [1-3]. However, during the use of mineral resources, a large amount of greenhouse gases will be produced, resulting in global warming. Thus, energy storage technology has attracted wide attention in the face of ecological degradation caused by the energy crisis [4-6]. It is recognized that the use of phase change energy storage can alleviate transient heat loads, balance the generation, and help to achieve carbon neutrality [7-10]. Nowadays, phase change energy storage technology has been widely used in the field of artificial environmental control, such as solar energy storage [11-14], power peak shaving and valley filling [15-17], building energy saving [18-21] and environmental control of underground evacuation facilities [22-24].

Over the past years, excellent progresses have been made with phase change energy storage technology in many energy-saving and sustainable energy applications for improving the energy efficiency [25-27]. The concept is not new but has attracted great attention in the application of air conditioning systems, ice storage air conditioning, as well as refrigeration system in the building and environment [28-31]. Dogan et al. [32] conducted a thermodynamic and economic study on the performance of the ice storage system integrated in the air conditioning system of large supermarkets. It was stated that the use of ice storage system could reduce the load of air conditioning by 47%. Fang et al. [33] developed an optimal seasonal ice storage device that can save 50% of the cooling electricity cost of residential buildings per year. Song et al. [34] studied the composite heat storage system combining chilled water heat storage and ice cold storage and investigated the influence of the ice storage volume on the economic feasibility of the composite system. Seyedeh et al. [35] proposed a wind-powered compression refrigeration cycle integrated with the system and conducted a dynamical study. Their results indicated that the daily coefficient of performance of the proposed system has grown 17% compared to the conventional cycle. Mohammad et al. [36] compared both the ice storage and phase-change material air conditioning system in office buildings with traditional one. Their results showed that the energy consumption of the ice storage and phase-change material air conditioning system was 4.59% and 7.58% lower than that of the traditional system, respectively. Xu et al. [37] proposed an experimental study to convert solar energy into electricity to provide the cooling power for ice storage air conditioning. Their results demonstrated that the utilization rate of the solar energy was 33.77%, while the cooling energy efficiency of the ice storage air conditioning system was 87.15%.

In recent years, phase change energy storage technology has been gradually applied to temperature control of the mine refuge chambers (MRCs). The MRC is a shelter space built in the surrounding rock underground and relatively isolated from the roadway environment. This space can provide a relatively safe environment for the survivors who cannot escape the disaster area after the mine accident to stay for at least 96 h [38,39]. It is noted that MRCs can play an important role in reducing the number of deaths from underground accidents [40,41]. Water vapor and heat generated by human metabolism during evacuation can make the thermal environment of the MRC to deteriorate [42]. Mine compressed air (MCA) would be a necessary ventilation measure, which can not only provide the necessary oxygen but also cool the ventilation of the low-temperature MRC [43]. However, when the initial surrounding rock temperature (ISRT) is above 27℃, it needs to be pointed out that the per capita MCA volume of 0.3 m^3/min could not meet the needs of the MRC to control the indoor air temperature below 35℃ within 96 h [44,45]. Over the past years, many technologies such as phase change cooling, liquid CO_2 cooling, and liquid air cooling have been developed for MRCs. The advantages of the phase change cooling are passive and maintenance-free, but for MRCs with ISRT higher than 24°C, pure phase change temperature control performance and economy are poor [46]. Liquid CO_2 refrigeration may leak and lose its refrigeration effect when the temperature is higher than 31.9℃, which limits its application [47]. Liquid air cooling technology has a wide range of application and high reliability but with high cost (500,000 ~ 700,000 Chinese yuan / set) [48].

Ice storage air conditioner has been widely used in temperature control of underground evacuation facilities due to its advantages of relative stability, no safety hazards, and low power consumption. Du et al. [49] designed a multi-functional ice storage air conditioning system that is suitable for 8-person rescue cabins. Their experimental results showed that the ice storage air conditioning can ultimately control the temperature and humidity of the rescue cabin at 31℃ and 77%. Wang et al. [50] developed an ice storage air conditioner with an ice storage volume of about 5.5 m^3. The hot air in the MRC can be driven by a circulating fan to flow through the heat exchange air duct to cool the living environment. It was found that the effective working time of the system is 64.57 h for a MRC occupied by 50 people. Xu et al. [51] proposed a non-electric cooling scheme that the encapsulated ice plate was placed directly in the chamber to control the indoor temperature. Their experimental result demonstrated that the ice storage plate with 633.5 kg could continuously maintain the temperature of the MRC below 35℃ within 72 h. Jia et al. [52] investigated the cooling application of the square ice storage boxes in the MRCs and they observed that the chamber with an initial temperature of 26℃ fluctuated at 29℃ after 24 h manned test. Zhang et al. [53] developed a novel temperature control scheme that combined the cold source storage with MCA, as shown in Fig. 1. The MCA pipe that entered the MRC was connected to a cold source storage device followed by cooling the MCA before it flowed into the living room. They stated that when the ISRT is 32℃, the ventilation with an air supply rate of 0.3 m^3/min per capita and a temperature of 20℃ could control the ambient temperature of the MRC below 35℃ within 96 h. Based on the novel temperature control scheme combining the cold source storage and MCA, the current work will design an ice storage cooling MCA device (ISCMCAD) for MRCs with high ISRT. It needs to be stressed here that the internal structure of the device will be the key factor affecting the heat transfer performance of ice storage air conditioning [54-58].

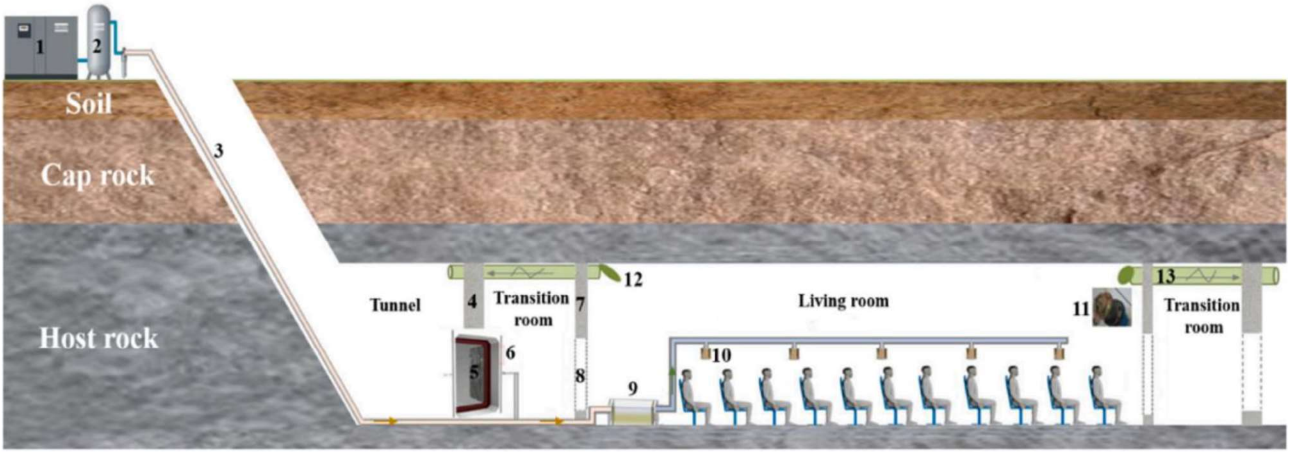

1 - Air compressor, 2 - Air storage tank, 3 - pipeline, 4 - Explosion-protection wall, 5- Protective airtight door, 6 - Air curtain, 7 - Seal wall, 8 - Airtight door, 9 - air cooling device, 10 - Silence air inlet, 11 - One-way exhaust valve, 12 - Air outlet, 13 - Exhaust outlet.

Fig. 1. Temperature control system of high-temperature MRC based on MCA and cooling device [53].

In summary, for MRCs with ISRT higher than 27℃, the temperature control goal cannot be achieved by MCA alone. Although the existing ice cold storage technology has good safety and a wide range of applications, it needs to be improved in terms of cost and reliability due to the reliance on explosion-proof fans and explosion-proof batteries. To the best of the authors' knowledge, the temperature control scheme combining MCA with ice storage is an economical and reliable option for MRCs with high ISRTs, yet no device has been developed for cooling the MCA. In the current work, a set of ISCMCAD combining the ice storage device with the MCA was designed for MRCs. An experimental platform is newly built to test the thermal performance of the ISCMCAD. Furthermore, a full-size numerical model of the ISCMCAD is developed and validated, and a sensitivity analysis is performed to investigate the effect of the heat exchange tubes' number (HETN), inlet air velocity (IAV) and inlet air temperature (IAT) on the heat exchange performance. In addition, a mixed air supply way is proposed to improve the utilization rate of cold storage capacity. The results can provide a theoretical guidance for the design and application of the ISCMCAD used in MRCs.

2. Material and method

2.1 Structural design calculation principle of ISCMCAD

2.1.1 Structure and principle

The ISCMCAD is composed of refrigeration compressor, ice storage tank, heat exchange tubes, copper tube, air buffer, air inlet and air outlet, and its structural principle is shown in Fig. 2 (a). The copper tube, coming from the refrigeration compressor is submerged in the ice storage tank by means of serpentine coils, then returns to the refrigeration compressor. The heat exchange tubes run through the air buffer in both sides. The air inlet will be connected to the MCA pipe, and the air outlet will be connected to the air supply end in the MRC. Fig. 2 (b) displays the actual ISCMCAD.

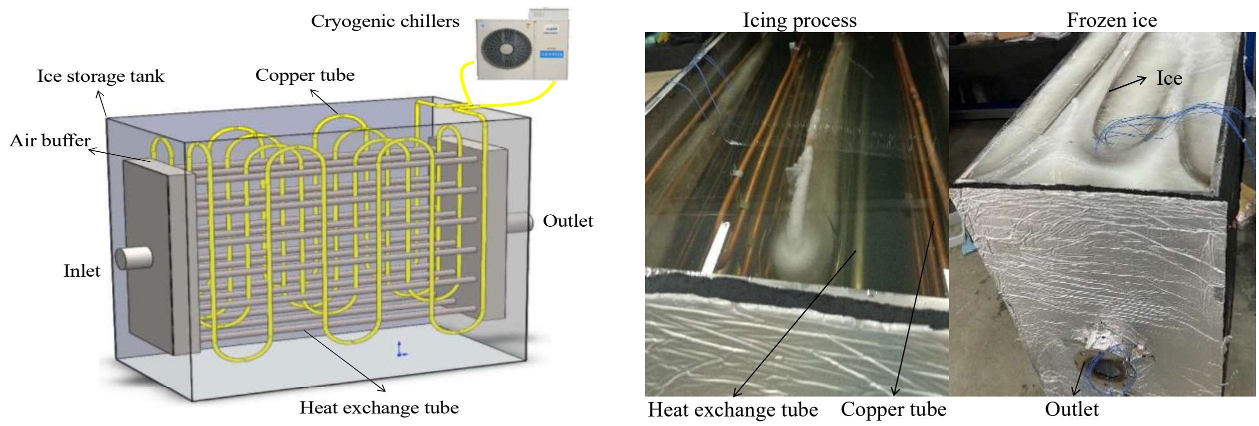

(a) Schematic diagram **(b) Physical diagram of ice storage**

Fig. 2. Schematic diagram and physical diagram of ISCMCAD.

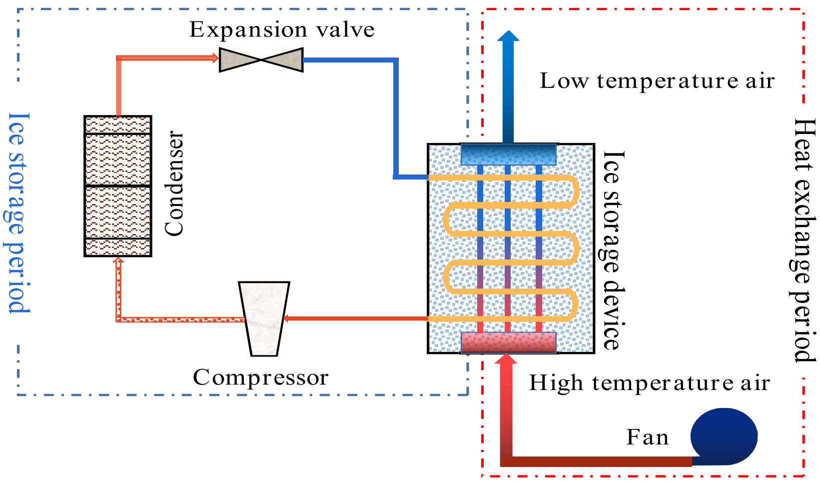

Fig. 3. Diagram of the operating principle of the ISCMCAD.

Fig. 3 shows the working principle of the ISCMCAD. During the ice storage period, the storage tank is filled with enough water, the refrigeration compressor is in the working state, the low-temperature refrigerant from the refrigeration compressor flows through the copper tube, and its cooling capacity cools water into ice through heat exchange. During the heat exchange period, the high-temperature MCA from the frequency conversion fan flows through a pipe into heat exchange tubes of the ISCMCAD, and becomes cold air via the heat exchange with walls of these heat exchange tubes, and the ice in the storage tank gradually melts into water due to the heat obtained from the MCA.

2.1.2 Cold storage capacity

In order to make it easy to carry the ISCMCAD to a MRC, the ice storage capacity of the ISCMCAD is designed to be 1 m^3 and the ice storage mass of 920 kg can be achieved. In the current work, the ice density of 920 kg/m^3 is used. The amount of the cold storage of the ISCMCAD can be calculated as follows [49].

$$Q_i = c_w \times \Delta t_w \times m_w + c_i \times \Delta t_i \times m_i + r_i \times m_i \tag{1}$$

Where, Q_i is the cold storage capacity (kJ), m_i is the mass of ice storage (kg), m_w is the mass of water storage in the ISCMCAD (kg), c_w is the specific heat capacity of water (J/kg·°C), Δt_w is the temperature difference of water (°C), c_i is the specific heat capacity of ice (J/kg·°C), Δt_i is the temperature difference of ice (°C), r_i is the latent heat of ice melting (J/kg).

The specific heat capacities of water and ice are 4200 J/(kg·°C) and 2100 J/(kg·°C) respectively, and the latent heat of ice melting is 3.35×10^5 J/kg. During the test, the temperature difference of water is 20°C, while the temperature difference of ice is 15°C. After substitute all the above values into Eq. (1), one can get Q_i = 414460 kJ.

Assume the heat dissipation of other equipment can be ignored, taking the heat dissipation capacity of 10 people in the MRC as an example, then the total heat load of the 96-hour MRC can be calculated as follows [59].

$$Q_r = q_r \times \tau \times n \tag{2}$$

Where, Q_r is the total heat load of the MRC (kJ), q_r is 120 J/s per capita heat dissipation power [59], τ is the time of refuge (h), n is the number of evacuees. According to Eq. (2), Q_r = 414720 kJ.

In terms of the calculation as above, it can be known that the cold amount of 1 m^3 ice can offset the heat emitted by 10 evacuees in 96 h. For a large MRC, multiple ISCMCAD can be equipped to meet cooling requirements. According to the size requirements of the door frame of the MRC, the ISCMCAD are normally designed to be 1.3 m in length, 0.7 m in width and 1.2 m in height, respectively. Moreover, referring to the diameter of the MCA duct, the diameter of the air inlet and air outlet of the ISCMCAD is set to 1m. The ISCMCAD will be installed in the transition room of the MRC and connected with the MCA duct. After the MCA is cooled by the ISCMCAD, it will be fed into the living room.

2.1.3 Calculation of the HETN

In the current study, the air is required to drop from 35°C to 20°C, given that the inlet speed of the ISCMCAD is around 10 m/s, the mass flow rate of the air can be obtained as 0.1013166 kg/s. Assuming that the number of the heat exchange tubes is 15, the air flow rate in the heat exchange tube can be found to be 7.41 m/s.

Logarithmic mean temperature difference (Δt_m) is calculated as follows [60].

$$\begin{cases} \Delta t_m = \dfrac{\Delta t' - \Delta t''}{\ln \dfrac{\Delta t'}{\Delta t''}} \\ \Delta t' = t_1 - t_w \\ \Delta t'' = t_2 - t_w \end{cases} \tag{3}$$

Where, t_w is the temperature of the pipe wall (°C), t_1 is the air inlet temperature (°C), and t_2 is the air outlet temperature (°C). In the present work, t_w is 0°C. Thus, the logarithmic mean temperature difference can be obtained by Eq. (3), which is Δt_m = 26.8°C.

The air heat transfer is calculated as follows [60].

$$Q_h = Mc_a(t_1 - t_2) \tag{4}$$

Where, Q_h is the air heat transfer (W), M is the air mass flow rate (kg/s), c_a is the specific heat capacity of air (kJ/kg· K). Here, c_a is 1.005 (kJ/kg·K). According to Eq. (4), the heat transfer Q_h = 1527.35 W can be obtained.

The surface heat transfer coefficient on the air side is calculated as follows [49,61].

$$k_1 = Nu \times \frac{\lambda_1}{d_1} \tag{5}$$

$$Nu = 0.023 \times \mathrm{Re}^{0.8} \times \mathrm{Pr}^{0.3} \tag{6}$$

$$\mathrm{Re} = \frac{u \times d_1}{\nu_1} \tag{7}$$

Where, k_1 is the surface heat transfer coefficient on the air side (W/m^2·K), Nu is the Nusselt number and it indicates the magnitude of the dimensionless excess temperature gradient of the wall normal vector, which reflects the strength of the convective heat transfer [49], Re is the Reynolds number, u is the air velocity in the heat exchange tube (m/s), d_1 is the inner diameter of the heat exchange tube (mm), λ_1 is the thermal conductivity of air (W/m· K), v_1 is the viscosity coefficient of the air motion (m^2/s), and Pr is the Prandtl number. According to the qualitative temperature of air Δt_m is 26.8°C, then the physical parameters of air can be obtained. The thermal conductivity of air is 2.52×10^{-2} (W/m · K), the viscosity coefficient of air motion is 15.37×10^{-6} m^2/s, Pr is 0.70236. According to Eqs. (5) - (7), the surface heat transfer coefficient of the air side k_1 = 36.93 W/m^2·K can be obtained.

The surface heat transfer coefficient on the ice-water side is calculated as follows [60].

$$k_2 = 0.725\times\left[\frac{\rho_2^{\ 2}\times\lambda_2^{\ 3}\times g\times r_i}{d_2\times\mu\times(t_i-t_w)}\right]^{\frac{1}{4}} \tag{8}$$

Where, k_2 is the surface heat transfer coefficient on the ice side (W/m^2·K), ρ_2 is the density of water (kg/m^3), λ_2 is the thermal conductivity of water (W/m· K), g is the acceleration of gravity (m/s^2), r_i is the latent heat of phase change of ice (J/kg), d_2 is the outer diameter of the heat exchange tube (mm), μ is the dynamic viscosity coefficient (N·s/m^2), t_i is the temperature of ice (℃), and t_w is the wall temperature of the heat exchange tube (℃). In the current work, ρ_2 is 999.9 (kg/m^3), λ_2 is 0.551 (W/m· K), g is 9.81 (m/s^2), r_i is 3.35×10^5 (J/kg), μ is 1788×10^{-6} (N·s/m^2), t_i is -15 (℃). From Eq. (8), the surface heat transfer coefficient of the ice side can be calculated k_2 = 3,592.31 (W/m^2·K).

The heat transfer coefficient of the heat exchange tube is calculated as follows [60].

$$k = \frac{1}{\frac{1}{k_1}+R_f+\frac{1}{k_2}} \tag{9}$$

Where, k is the heat transfer coefficient of the heat exchange tube (W/m^2·K), k_1 is the surface heat transfer coefficient on the air side (W/m^2·K), R_f is the thermal resistance of the dirt (m^2·K/W), and k_2 is the surface heat transfer coefficient on the ice side (W/m^2·K). From Eq. (9), the heat transfer coefficient of the heat exchange tube k = 36.28 W/m^2·K can be found.

The total heat transfer area of the heat exchange tube is calculated as follows.

$$A = \frac{Q_h}{k\times\Delta t_m} \tag{10}$$

Where, Q_h is the air heat transfer (W), k is the heat transfer coefficient of the heat exchange tube (W/m^2·K), and Δt_m is the logarithmic mean temperature difference (°C). According to Eq. (10), the total heat transfer area of heat exchange tubes A = 1.78 m^2 is obtained.

The number of heat exchange tubes is calculated as follows.

$$N = \frac{A}{\pi d_2 L} \tag{11}$$

Where, A is the total heat transfer area of the heat exchange tube (m^2), d_1 is the outer diameter of the heat exchange tube, and L is the length of a single heat exchange tube. According to Eq. (11), N = 15.15 can be obtained. The error from the hypothetical value is only 1%, indicating that the HETN is reasonably designed. It can be calculated that for the ISCMCAD, the HETN is at least 15, to cool the air temperature from 35℃ to 20℃. For the experimental ISCMCAD, the HETN is 18, the heat exchange tube has a length of 1.1 m, an inner diameter of 30 mm and a wall thickness of 2 mm.

2.1.4 Evaluation indexes for the ISCMCAD

In order to evaluate the heat transfer performance of ISCMCAD, two evaluation indexes: ice storage utilization rate η% and outlet air temperature (OAT) variance R^2 are introduced. The ice storage utilization rate of η% indicates the percentage of ice melted by the ISCMCAD after 96 h of heat exchange, while the OAT variance R^2 indicates the stability of the ISCMCAD during heat exchange. The theoretical ice storage capacity of the ISCMCAD is 1 m^3 and the safety factor of 1.2 times should be considered in practical applications. The actual ice storage amount should be 1.2 m^3. Thus, when the volume of the ice is 1 m^3, the utilization rate of the melted ice can be calculated as follows.

$$\eta_{ind} = \frac{V_{the}}{V_{act}} \times 100 \tag{12}$$

$$\eta = \frac{V_{mel}}{V_{tot}} \times 100 \tag{13}$$

Where, η_{ind} is the ice storage utilization index (%), V_{the} is the theoretical amount of the ice storage (m^3), V_{act} is the actual amount of the ice storage (m^3), V_{mel} is the amount of the ice melt during heat exchange in the ISCMCAD (m^3), and V_{tot} is the total ice storage capacity of the ISCMCAD (m^3). From Eq (12), η_{ind} = 83.33% can be obtained, and when η > 83.33% after 96h heat exchange, it indicates that the utilization rate of the ISCMCAD is satisfied.

The variance of OAT within 96 h is calculated as follows.

$$R^2 = \frac{\sum_{j=1}^{n} (t_j - \bar{t})^2}{n} \tag{14}$$

Where, R^2 is the variance of the OAT, t_j is the OAT at time j, and $\bar{t}$ is the average temperature of the

OAT within 96 h. The smaller the variance of the OAT, the more stable the heat exchange of the ISCMCAD within 96 h.

2.2 Experiment detail

2.2.1 Experimental environment and principle

The experimental platform mainly includes the temperature control room and the ISCMCAD, as shown in Fig. 4. The temperature control room has a size of 3.6 m × 3.1 m × 3.0 m, in which the air temperature can be controlled within the range of 20 ~ 60℃ with a relatively stable value through a temperature control system. The ISCMCAD is placed outside of the temperature control room, and connected to the temperature control room by an air pipeline an inner diameter of 0.1 m. To make the hot air in the temperature control room enter the heat exchange tubes of the ISCMCAD, a frequency conversion fan is placed in the temperature control room, the fan can control the wind speed of the air pipeline ranging from 0 to 30 m/s. The specific parameters are listed in Table 1.

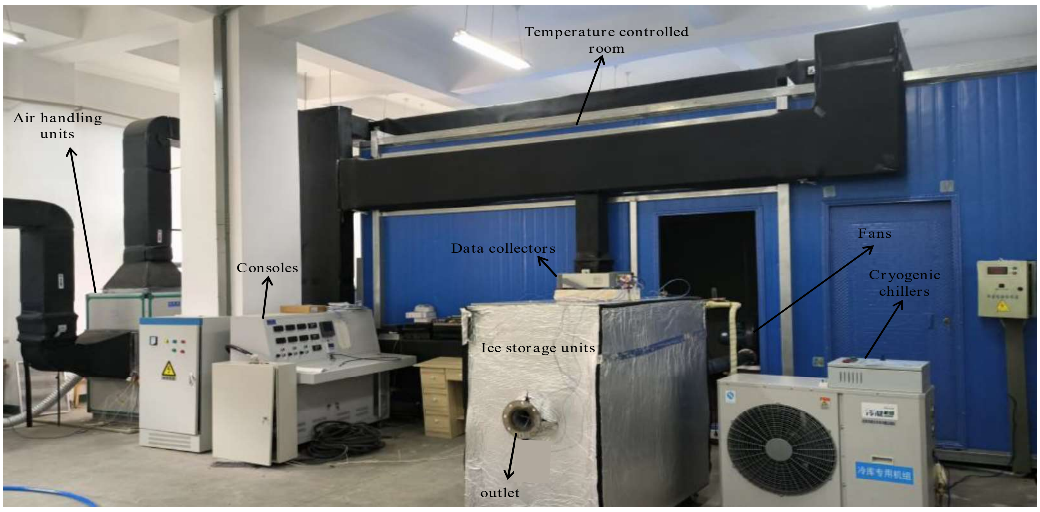

Fig. 4. Experimental platform.

Table 1. Table of main experimental equipment parameters

Device name	Device parameters	Remarks
ISCMCAD	1.3 m×0.70 m×1.2 m	Covered by insulation cotton with a thickness of 30 mm
Inverter fan	Rate of flow: 1530 m^3/h Power: 1.5 Kw Voltage: 380 V	Equipped with a frequency converter to control the wind speed
Cryogenic chiller	Cryogen: R22 Evaporation temperature: -12 ~ 10℃ Cooling capacity: 14 kW	/

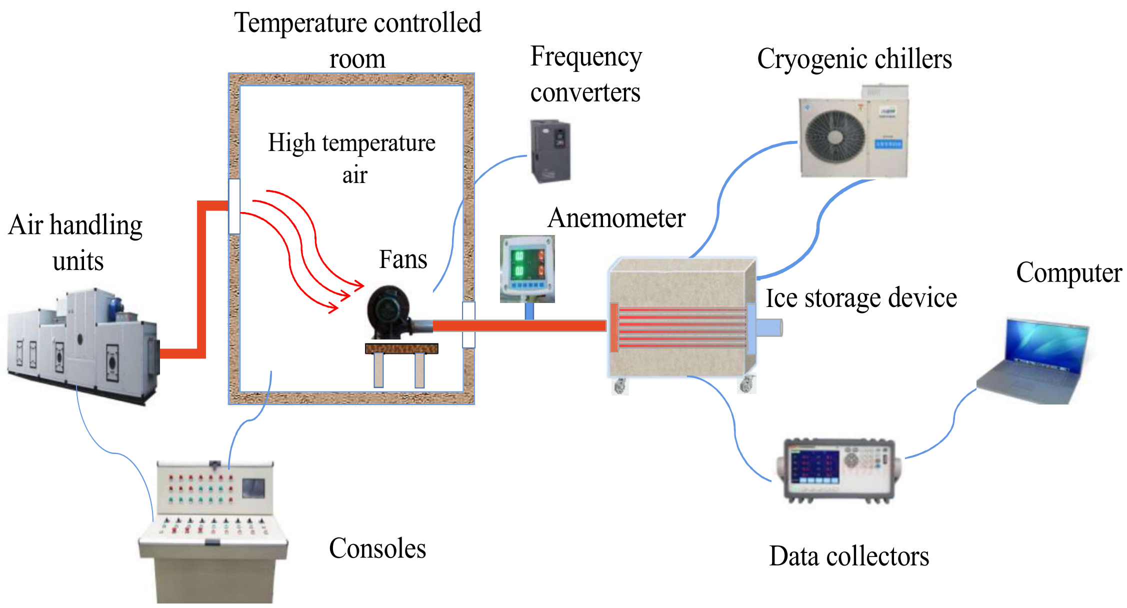

Fig. 5. Experimental principle.

Fig. 5 demonstrates the experimental principle. During the ice storage period, the monitoring points arranged in the ISCMCAD can monitor the ice storage characteristics of the device. Considering that water will expand when it freezes, 10% of the expansion space will be reserved. Inject 90% of the water into the ice storage device and then turn on the low-temperature refrigerator to make the water in the device into ice. In the heat exchange period, after the ice storage is completed, the air handling unit is first turned on to send hot air to the temperature control room. Adjust the supply air temperature of the air handling unit through the console until the indoor temperature stabilizes at the experimental set temperature, and then turn on the fan to send high-temperature air into the ISCMCAD for heat exchange and cooling.

2.2.2 Data collection

Fig. 6 displays the arrangement of the temperature monitoring points. There are 20 points evenly arranged on the storage tank. Among them, 6 points are arranged at the 0.3 m and 0.9 m levels, and 8 points are arranged at the 0.6 m level. To measure the air temperature, there are 1 monitoring point at the air inlet and 3 monitoring points at the air outlet. These measuring points are measured by K-type thermocouple with a measuring range of -200 ~ 1800°C and an accuracy of 0.01°C. The monitoring data is automatically recorded once a minute by a temperature collector. The relative humidity is monitored by a hygrometer, and the IAV is monitored by an anemometer. Before the experiment begins, the thermocouples will be calibrated through a mixture of ice water at 0°C. Table 2 lists the parameters of the instruments.

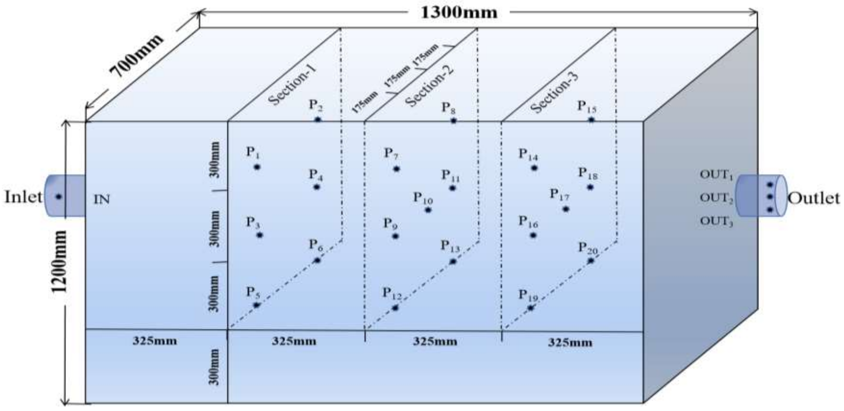

Fig. 6. Temperature measurement point arrangement

Table 2 Data acquisition instrument parameter

Name	Model	Range	Accuracy	Remarks
Temperature collector	JK4000	-200 ~ 1800℃	0.01℃	Work environment: 20% ~ 90% RH
Thermocouple	K-type	-200 ~ 1800℃	± 0.01℃	/
Anemometer	LSFS-4	0 ~ 9000 m^3/h	0.02%	Work environment: -40 ~ 80℃

2.2.3 Experimental conditions

To control the air quality, a MRC needs to keep the air delivery volume (ADV) at least 0.3 m^3/min per capita [62]. In the case of 0.3 m^3/min per capita, when the ISRT was 30, 31, 32, 33 and 34℃, the ventilation temperature was 23.28, 21.83, 20.38, 18.93 and 17.48℃, respectively, according to ref. [53]. Therefore, The ISCMCAD needs to meet the air supply requirements per capita while meeting the cooling requirements. Taking the MRCs that can accommodate 10 and 15 people as an example, it can be concluded that the IAV of the ISCMCAD is 7 m/s and 10 m/s, respectively. In order to study whether the cooling of the ice storage cooling device can meet the requirements of the air supply temperature of the refuge chamber. The following two groups of working conditions were selected for experiments: Case 1: IAT is 31°C, IAV is 7 m/s, Case 2: IAT is 32°C, IAV is 10m/s.

2.2.4 Data processing

During the experiment, there is a certain fluctuation range of the IAT of the ISCMCAD since it is difficult to keep the ambient temperature as constant. In this case, it would affect the accuracy of the OAT of the ISCMCAD. In order to reduce the error caused by the IAT fluctuation, the data with the IAT fluctuation less than 0.5°C is selected. In addition, the concept of the inlet and OAT difference and average outlet temperature(AOT) are introduced to analyze the heat exchange performance of the ISCMCAD in order to further improve the reliability of the experimental data.

The uncertainty analysis for the direct measurement can be calculated as follows [63,64].

$$u_1 = \sqrt{\frac{\sum_{i=1}^{n}(\mathrm{T}_i - \overline{\mathrm{T}})^2}{n(n-1)} + (\frac{\Delta_s}{3})^2} \tag{15}$$

Where, u_1 is the uncertainty of the direct measurement result, n is the number of measurements, T_i is the measurement data, $\bar{T}$ is the average value of the measurement data, and Δ_s is the measurement error of the instrument.

Whereas the uncertainty analysis of the indirect measurement results can be calculated as follows [63,64].

$$U_2 = \sqrt{\sum_{n=j}^{n}(\frac{\partial f}{\partial x_j})^2 \times u_j^{\ 2}} \tag{16}$$

Where, U_2 is the uncertainty of the indirect measurement result, n is the number of parameters related to the indirect measurement result, x_j is the parameter of the direct measurement, f is the calculation function, and u_j is the uncertainty of the direct measurement parameter.

Taking experimental case 1 as an example, after 96 hours of testing, the direct measurement results of the temperature at the three measuring points in the outlet are 24.2℃, 24.7℃, and 24.6℃, respectively, and the error of the instrument measurement is 0.01℃. According to Eq (15), the uncertainty of the direct measurement result of the outlet air temperature is 0.15°C. Calculate the uncertainty of the indirect measurement results with the temperature difference between the inlet and outlet. The inlet and outlet temperature difference can be expressed as $f=T_{in}-T_{out}$, then the uncertainty of the outlet temperature is 0.15℃ while the uncertainty of the inlet temperature is 0.088℃. According to Eq (16), the uncertainty of the indirect measurement of the temperature difference between the inlet and outlet is 0.17℃. Similarly, the uncertainties of other related parameters can be calculated.

2.2.5 Experimental Procedures

In the current work, the main experimental steps are listed as follows:

(1) Arrange the temperature measurement point in the ISCMCAD and set the recording interval of the data acquisition instrument to 1 min each time;

(2) Ice storage stage: considering the volume expansion characteristics of the water icing, the ISCMCAD is filled with 90% water, and after checking and confirming that the device is not leaking,

turn on the Cryogenic chiller to freeze the water into ice, and monitor the ice storage in the device in real time through the temperature measurement point in the device. Turn on the data collector and connect to the computer to record the ice storage experimental data;

(3) Heat exchange and cooling stage: in the ISCMCAD, after the water is completely frozen into ice and the temperature in the device is below -15℃, then turn off the Cryogenic chiller, arrangement of temperature measuring points at the inlet and outlet of the ISCMCAD and arrangement of wind speed measurement points at the inlet;

(4) Start the full air handling unit to adjust the supply air temperature and send the high-temperature air into the temperature control room for heating, and adjust and control the IAT;

(5) When the temperature in the temperature control room reaches the dynamic balance, set the experimental IAV and turn on the frequency conversion fan to adjust the IAV;

(6) Turn on the data collector and connect it to the computer to record the cooling experiment data of the ISCMCAD, and turn off the system after running for 96 h;

(7) Data collection and analysis.

2.3 Computational details

2.3.1 Computational model and meshing

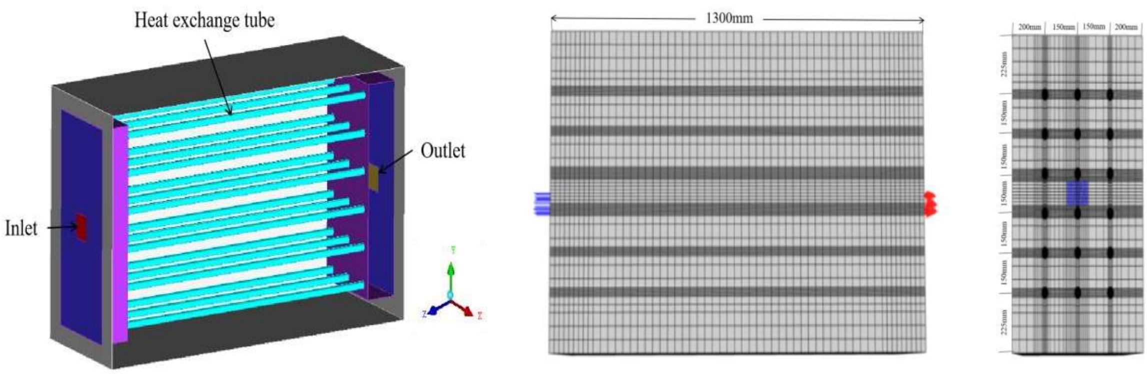

(a) Numerical model **(b) Grid division**

Fig. 7. Numerical model of ISCMCAD.

This section mainly studies the heat transfer process between the hot air and the ice when passing through the heat exchange tubes, the copper tube does not participate in the heat transfer process, so it is not arranged in the computational model. The computational model of the ISCMCAD is meshed by ANSYS ICEM and the structural grid is adopted, as shown in Fig. 7. The size of the ISCMCAD, the HETN, the IAV, the IAT, and the material of the heat exchange tubes are consistent with the experimental device. The inner diameter of the heat exchange tube is 30 mm, the HETN is 18, and the tube spacing along the X and Y direction is 150 mm. The computational model has two fluid zones. To reduce the computational error of the coupling interface of the two fluid zones and better capture the characteristics of the temperature field during the calculation process, the number of grids on surfaces such as coupling walls, heat exchange tube walls, air inlets and outlets are increased. In the current work, a grid independence study is carried out and 6 different grid numbers, i.e., 543625, 856423, 126845, 1268456, 1865267, 2687625 and 3215648 are selected. The numerical results of the case with an IAT of 32°C and an IAV of 10 m/s are selected for the comparison. Fig. 8 plots the air temperature change of the air outlet of the ISCMCAD device at different times under different grid numbers. It can be observed that the OAT value changes greatly when the number of grids is lower than 1865267, after which increasing the number of grids has little effect on the temperature value. Therefore, a grid number of 1865267 with a grid quality of 0.73 is selected for the following numerical simulation.

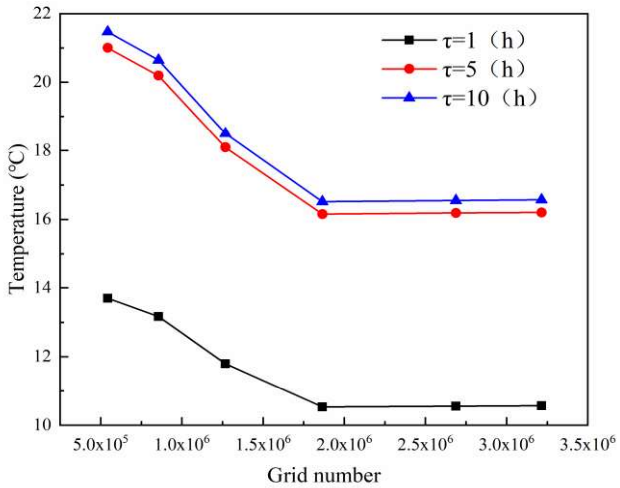

Fig. 8. Effect curve of different grid numbers on OAT.

2.3.2 Initial Conditions and Boundary Conditions

In the present work, the control variable method is used to study the effects of different IAT, IAV and HETN on the heat transfer performance of ISCMCAD. When the ISRT is higher than 27°C, the original MCA is difficult to meet the temperature control requirements of the MRC. For the cases of the ISRT is 30, 31, 32, 33 and 34°C, the ventilation temperature needs to be cooled to 23.28, 21.83, 20.38, 18.93 and 17.48°C correspondingly in order to meet the cooling requirements of the MRC within 96 h [53]. Since the pressurized air is fully exchanged with the surrounding rock during the flow into the MRC, the temperature of the MCA is close to the ISRT, thus the IAT of the ISCMCAD needs to be set to 30, 31, 32, 33 and 34°C. According to the temperature difference of the ADV and the Q_i of the ISCMCAD, the supply air velocity of MRC can be found between 5 ~ 15 m/s, therefore, the IAV is set to 5, 7.5, 10, 12.5 and 15 m/s. The specific numerical case studies are listed in Table 3.

Table 3 Numerical simulation case studies.

Case	IAV（m/s）	IAT（℃）	HETN
1	10	32	6
2	10	32	9
3	10	32	12
4	10	32	15
5	10	32	18
6	5	32	18
7	7.5	32	18
8	12.5	32	18
9	15	32	18
10	10	30	18
11	10	31	18
12	10	33	18
13	10	34	18

The air inlet is set to be the velocity inlet, while the air outlet is set to the pressure outlet. The interface between the air watershed and the ice-water watershed is set to be a coupled heat transfer wall, and the other walls are set as an insulated wall. The wall and other wall materials of the heat exchange tubes are made of steel, and the thickness of each wall is set to be 2 mm.

2.3.3 Turbulence model

Since the solidification and melting characteristics as well as the heat transfer properties of the ice cannot be visualized during the experiment, in order to capture the changes of the interface during ice solidification and melting, the enthalpy-porosity method is developed. The computational domain is considered to be a porous region where the volume fraction of the liquid is similar to porosity. The volume fraction will be 0 when the water is completely solidified, while a volume fraction is 1 when the ice is completely melted. This method has been widely used in other studies to solve the solidification and melting problems [65]. Yang et al. [66] simulated the heat transfer of the circular phase-change material air heat exchange by using the renormalization group RNG κ-ε model and the enhanced wall treatment method. Their simulation results were in good agreement with the experimental data. In the present work, the solidification and melting model, RNG κ-ε turbulence model and enhanced wall treatment method is used to simulate the air heat transfer in the tube. Several assumptions are made to simplify the model: (1) the liquid is Newtonian fluid and incompressible, (2) the over-cooling and volume expansion of the water during solidification are ignored, (3) the heat loss through the outer wall of the ISCMCAD is not considered, and (4) the flowing air in the heat exchange tube is dry air. In addition to density, the thermophysical properties of water are set to different constant values, and the density of water depends on temperature expressed as follows[67]:

$$\rho = \rho_{\max}(1-\xi\left|T-T_{\max}\right|^{1.89}) \tag{17}$$

Where, ρ is the density of water (kg/m^3), ρ_{max} is the maximum density, and T_{max} is the temperature at the maximum density (℃). In the current study, ρ_{max}=1000 kg/m^3, ξ=9.3×10-6, T_{max}=4 ℃.

The mass conservation equation is expressed as follows [67]:

$$\frac{\partial\rho}{\partial\tau}+\nabla\cdot(\rho\vec{V})=0 \tag{18}$$

Where, $\vec{V}$ is the velocity vector (m/s) and τ is the time (s).

The momentum conservation equation is expressed as follows [68]:

$$\rho\frac{\partial\vec{U}}{\partial\tau}+\rho(\vec{V}\cdot\nabla)\vec{V}=-\nabla p+\mu\cdot\nabla^2\vec{V}+\rho\alpha(T-T_{ref})\vec{g}+\vec{S} \tag{19}$$

$$S=\frac{(1+\gamma)^2}{(\gamma^3+\omega)}C_{\mathrm{m}}\vec{V} \tag{20}$$

Where, p is the pressure (Pa), μ is the coefficient of dynamic viscosity (N·s/m^2), and α is the coefficient of thermal expansion (1/K), $\vec{g}$ is the gravity acceleration (m/s^2), $\vec{S}$ is the source term (m/s) used to account for changes in fluid velocity during solidification, γ is the liquid volume fraction, ω is the small value (0.001) to avoid division by zero, C_m is the mushy zone constant usually set in the range $1\times10^4\sim1\times10^7$ kg/(m3·s). In the current study, C_m is assumed to be a constant value of 1×10^6 kg/(m3·s) [69].

The energy conservation equation is expressed as follows [68]:

$$\frac{\partial H}{\partial\tau}+\nabla\cdot(\vec{V}h_{sens})=\nabla\cdot(\frac{k}{\rho c_p}\nabla h_{sens}) \tag{21}$$

$$H=h_{sens}+\Delta h \tag{22}$$

Where, H is the total enthalpy change value during the heat transfer, h_{sens} is the sensible enthalpy of the material (kJ/kg), and Δh is the enthalpy of the phase transition of the material (kJ/kg). The values of h_{sens} and Δh can be calculated from Eqs. (23) and (24) [68]:

$$h_{sens} = h_{ref} + c_p \int_{T_{ref}}^{T} dT \tag{23}$$

$$\Delta h = \sum_{i=1}^{n} \beta_i E \tag{24}$$

Where, h_{ref} is the enthalpy of the reference surface (kJ/kg), T_{ref} is the temperature value of the reference surface (°C), E is the enthalpy of the phase transition of the unit material (kJ/kg), and γ is the liquid volume fraction, it can be calculated as follows [68]:

$$\gamma = \begin{cases} 0 & T < T_{solid} \\ \dfrac{T - T_{solid}}{T_{liquid} - T_{solid}} & T_{solid} < T < T_{liquid} \\ 1 & T > T_{liquid} \end{cases} \tag{25}$$

The κ and ε transport equations for the RNG κ-ε model are as follows [63]:

$$\frac{\partial}{\partial \tau}(\rho k) + \frac{\partial}{\partial x_i}(\rho k u_i) = \frac{\partial}{\partial x_j}\left[\alpha_k \mu_{eff} \frac{\partial k}{\partial x_j}\right] + G_k + G_b - \rho\varepsilon - Y_M + S_k \tag{26}$$

$$\frac{\partial}{\partial \tau}(\rho \varepsilon) + \frac{\partial}{\partial x_i}(\rho \varepsilon u_i) = \frac{\partial}{\partial x_j}\left[\alpha_\varepsilon \mu_{eff} \frac{\partial \varepsilon}{\partial x_j}\right] + C_{1\varepsilon}\frac{\varepsilon}{k}(G_k + C_{3\varepsilon} G_b) - C_{2\varepsilon}\rho\frac{\varepsilon^2}{k} - R_\varepsilon + S_\varepsilon \tag{27}$$

Where, G_k represents the turbulent energy term generated by the laminar velocity gradient, G_b is a term of turbulent kinetic energy generated by buoyancy, Y_M represents the contribution of the turbulent pulsation expansion to the dissipation rate in the entire process in compressible flow. In compressible flow, C_1, C_2, and C_3 are constants, and S_k and S_ε are user-defined turbulent kinetic energy terms and turbulent dissipation terms.

2.3.4 Numerical simulation parameters

In the current work, numerical simulations are carried out using commercial ANSYS Fluent software. The pressure-speed coupling separation algorithm based on SIMPLE pressure is adopted, and the second-order style formula is adopted to ensure the numerical accuracy. The relaxation factor remains unchanged and the simulation is convergent when the residual differences of mass, momentum and energy are less than 1×10^{-3}, 1×10^{-3} and 1×10^{-6}. As shown in Fig. 9, it can be found that when the time step is less than 2 s, changing it has almost no effect on the calculation result, but after that, the calculation result changes significantly as it increases. Therefore, for the following numerical simulation, the time step is set as 2 s.

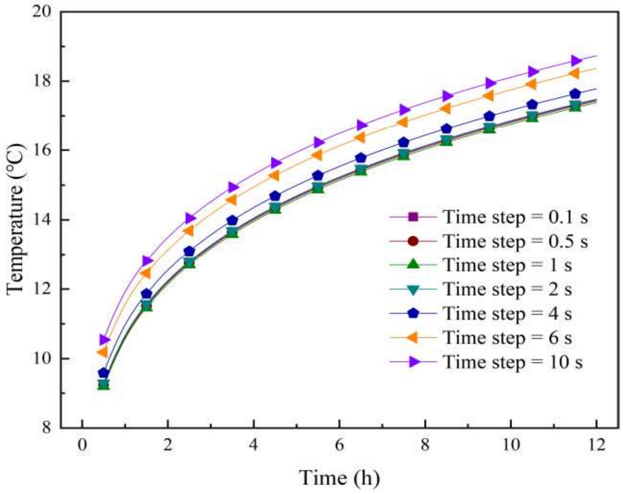

Fig 9. Effect curve of different time steps on OAT.

2.3.5 Model validation

To verify the accuracy and reliability of the numerical model, two case studies, IAT 31℃, IAV 7 m/s, and IAT 32℃, IAV 10 m/s, are selected. The numerical condition keeps the same as the experimental condition.

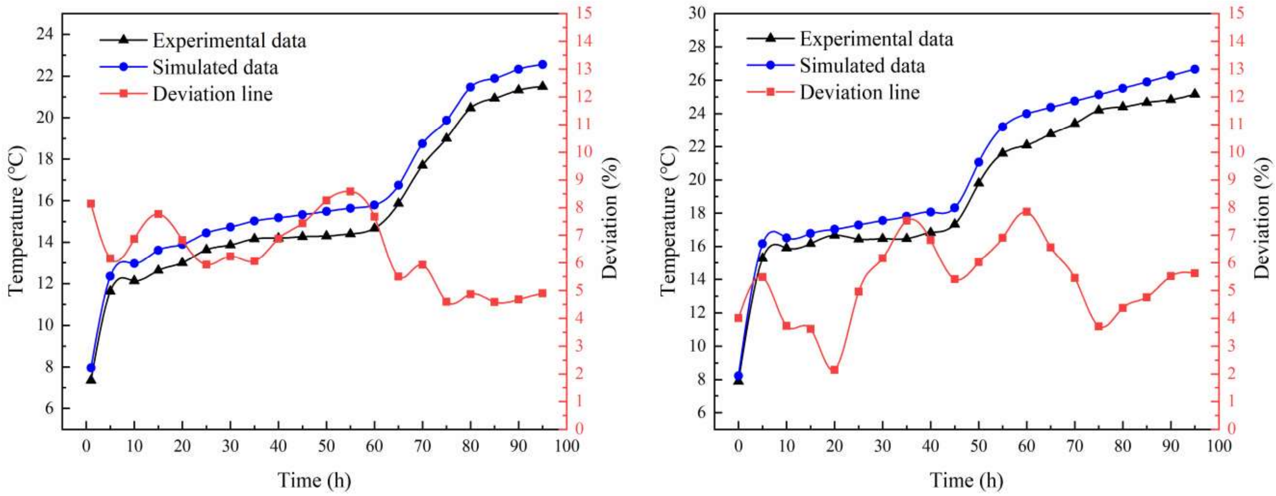

(a) IAT=31℃, IAV=7 m/s **(b) IAT=32℃, IAV=10 m/s**

Fig. 10. Comparison of the OAT between experimental and numerical results.

Fig. 10 compares the variation of the OAT with time within 96 hours between the experimental data and simulation results. It can be observed that for these two cases, the temperature trend of the numerical data is in good agreement with that of the experimental data. During the 96-hour period, the temperature difference of the air outlet between the numerical results and the experimental results is always less than 1.2°C, and the deviation is less than 10%, within the acceptable range, indicating that the numerical model is reliable for the following numerical simulation.

3. Results

3.1 Heat transfer performance of the ISCMCAD

3.1.1 Ice storage characteristics

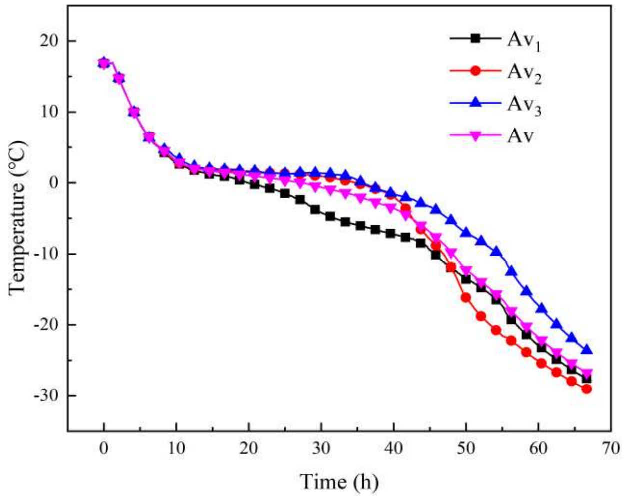

Fig. 11. Ice storage performance curve of the ISCMCAD

The temperature change profile in the device during ice storage is plotted in Fig. 11. Av_1, Av_2 and Av_3 are the average temperatures of the measurement points on section 1, section 2 and section 3 of the ISCMCAD, respectively. Av is the average temperature of all measurement points in the ISCMCAD. It can be found that during refrigeration, the temperature of monitoring points in the tank decreases over time, and the temperature drop process can be roughly divided into three stages. During the first 10 hours, the measuring temperature drops rapidly and linearly from 16℃ to about 2℃. However, from 10 to 35 hours, the temperature drops rate decreases significantly, dropping by only about 2℃, because phase change endothermic dominates during this period, and most of the cold energy is absorbed from water to ice. After 40 hours, the water basically solidifies with the temperature of below -1℃, and the measuring point resumes a rapid downward trend due to the storage of cold energy through sensible heat. At 65 h, the ice temperature drops to -15℃. Thus, it can be deduced that the ice storage function of the device can be completed within 2 ~ 3 days, accompanied by the water temperature being frozen to -15°C.

3.1.2 MCA cooling characteristics

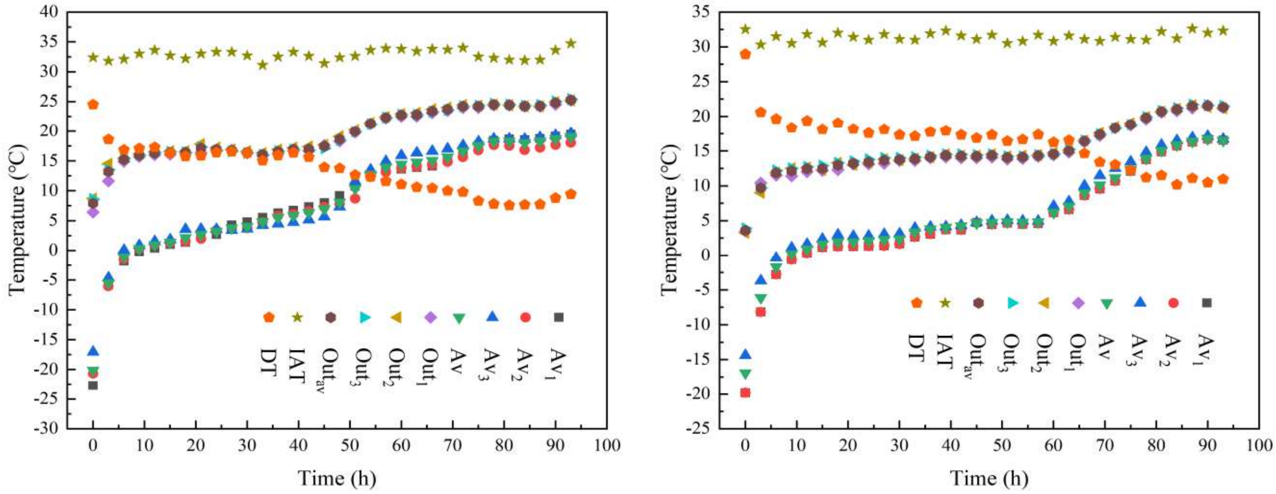

(a) IAT=32℃, IAV=10 m/s **(b) IAT=31℃, IAV=7 m/s**

Fig. 12. Cooling performance curve of ISCMCAD

Fig. 12 plots the OAT profile of the ISCMCAD within 96 h and the temperature profile of the ice-water mixture in the ISCMCAD under two case studies: IAT of 32℃, IAV of 10m/s and IAT of 31℃, IAV of 7 m/s. Here, Out_1, Out_2 and Out_3 are the temperatures of the three measurement points at the air outlet, respectively, Out_{av} and DT are the average temperature of the outlet and the temperature difference between the air inlet and the air outlet. From Fig. 12, it can be found that the OAT increases with the increase of time, which is basically consistent with the trend of the temperature change of the ice-water mixture in the ISCMCAD during the whole 96 h heat exchange process. As shown in Fig. 12 (a), for the case of the IAV is 10 m/s and IAT is 32℃, the ISCMCAD is capable of cooling the temperature of air volume rate required by 15 people to below 24.5℃ within 96 h. The entire heat exchange period can be divided into four stages: 1) the first stage is mainly cooled by the exchange of sensible heat between ice and air, the OAT of the ISCMCAD increased from 7.9℃ to 15.28℃, 5 h before the heat exchange and the temperature rises by a large margin; 2) the second stage is mainly cooled by the latent heat exchange between the air and ice melting, at the same time, it is accompanied by sensible heat exchange between air and water. During the 5 ~ 45 h period, the OAT rises from 15.28℃ to about 17.33℃, and the temperature rises gently; 3) the third stage, covering 45 to 55 h, is mainly influenced by the sensible and latent heat exchange of the well mixed water and ice, most of the ice melt due to the rising water temperature, leading to the OAT rises relatively quickly; and 4) the fourth stage is mainly the sensible heat exchange between the air and water, after 55 h, the OAT of most ice melts rose quickly, and the OAT was 24.5℃. As shown in Fig. 12 (b), for the case of the IAV is 7 m/s and the IAT is 31℃, the ISCMCAD can reduce the air temperature below 21.5°C within 96 h, the first 10 h during the heat exchange period of the ISCMCAD is the first stage, which is mainly cooled by the sensible heat exchange between the air and ice, the OAT was increased from 3.57°C to 12.33°C. Between 10 and 60 h is the second stage, mainly cooled by the latent heat exchange between air and ice melting, the OAT rises from 12.33°C to 14.63°C. The third stage, between 60 and 70 h, the air is mainly exchanged by sensible heat with water and latent heat exchange with ice. The fourth stage, after 70 h which is mainly cooled by the sensible heat exchange between the air and water, and the OAT of the ISCMCAD is within 21.5°C after 96 h heat exchange and cooling. It can be concluded that when the IAV is 10 m/s and the IAT is 32°C, the IAT of the ISCMCAD after 96 h the heat exchange is about 7.5°C and the average temperature difference at the outlet is 19.61°C. When the IAV is 7 m/s and the IAT is 31°C, the IAT of the ISCMCAD is about 10°C and the average temperature difference at the air outlet is 16.78°C. According to Eqs. (5) and (10), under different IAV, the heat transfer coefficient of the ISCMCAD ranges from 24.26 to 36.28 W/m^2·K.

3.2 Numerical analysis of typical case

In order to obtain the change of the water-ice temperature and the OAT in the ISCMCAD during the 96 h heat exchange, the numerical simulation results of the IAT of 32°C, the IAV of 10 m/s and the HETN of 18 are selected for analysis.

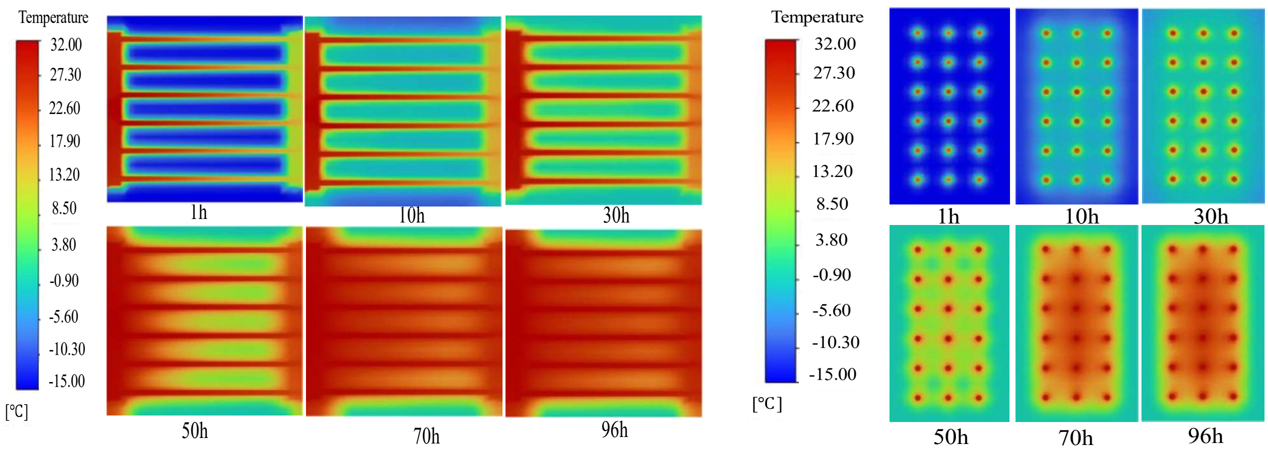

(a)Y - Z section **(b) X - Y section**

Fig. 13. **Heat transfer temperature distribution of ISCMCAD.**

Fig. 13 shows the temperature distribution of the ISCMCAD at five different times 1, 10, 30, 50, 70 and 96 h. It can be seen that the OAT of the ISCMCAD increases with time, and the OAT rises rapidly during 1 ~ 10 h, mainly influenced by the sensible heat exchange of ice. However, from 10 to 50 h, the OAT rises slowly, the ice around the heat exchange gradually begins to melt, mainly influenced by the latent heat exchange from melting ice, the OAT ranges from 16℃ to 18℃. At 50 h, the temperature around the heat exchange bundle is above 2℃, indicating that the ice melting around the heat exchange is complete. When the time reaches 70 h, the OAT increases significantly but not higher than 25.96℃ within 96 h.

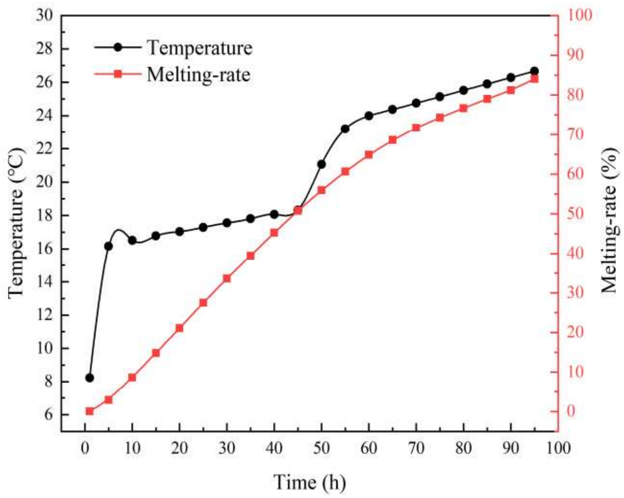

Fig. 14. Heat transfer performance curve of ISCMCAD.

Fig. 14 plots the profiles of OAT of the ISCMCAD and the ice storage melting. It can be observed that the OAT and the ice melting rate (IMR) increase with time, and the change in OAT can be divided into four stages. The first stage, ranging from 0 to 5 h, is mainly influenced by the sensible heat exchange of the rising ice temperature, the OAT of the ISCMCAD increases from 8.23℃ to 16.15℃. The second stage, between 5 and 45 h, is mainly influenced by the latent heat exchange of ice melting, the OAT rises gradually from 16.15℃ to 18.32℃. The third stage, from 45 to 55 h, is mainly influenced by the sensible and latent heat exchange of the well mixed water and ice. Most of the ice melting due to the rising water temperature, which leads to the OAT rising quickly. The reason for this phenomenon is that after 45 h heat exchange, the ice melts approximately 50%, meaning that the ice around the heat exchange tubes has melted completely, the latent heat absorbed by the melting ice in the unit has little effect on the OAT. The fourth stage, from 55 to 96 h, is mainly influenced by the sensible heat exchange of the rising water temperature. At the time of 96 h, the OAT is 25.96℃ with the ice melting about 85%.

3.3 Sensitivity analysis

3.3.1 Effect of the HETN

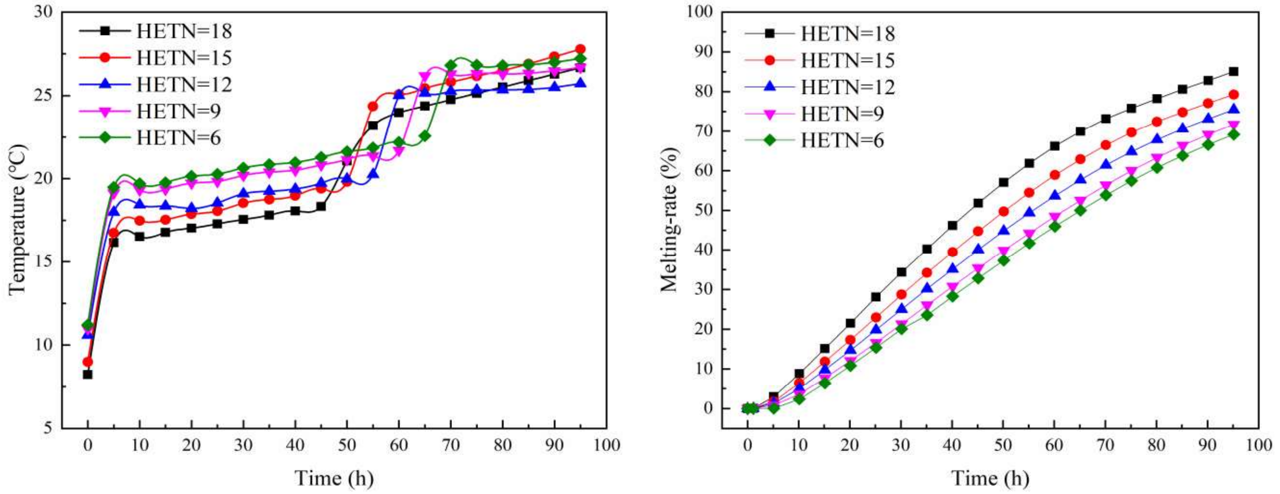

(a) OAT change curve **(b) IMR curve**

Fig. 15. Heat transfer performance curve of ISCMCAD with different HETNs at IAT of 32℃ and IAV of 10m/s.

Fig. 15 demonstrates the effect of different HETN on the OAT and melting rate of the ISCMCAD at IAT of 32°C and IAV of 10 m/s. As shown in Fig. 15 (a), it is noted that the OAT of the ISCMCAD decreases with the increase of the heat transfer tube bundle in the first 50 h, this is attributed to the increase of the heat transfer area with more tubes. As HETN decreases, the time of latent heat transfer increases, mainly because the reduction of HETN not only makes the heat transfer area smaller, but also increases the amount of ice between adjacent tubes. The AOT of the ISCMCAD with the number of tubes of 18, 15, 12, 9 and 6 during the 96 h heat exchange period are 20.53, 21.37, 21.13, 21.96 and 22.21°C, respectively. It can be concluded that the cooling effect of the ISCMCAD with the HETN of 18 is better. According to Eq. (14), the OAT variance of ISCMCADs with 18, 15, 12, 9 and 6 HETN during the 96 h heat transfer period is 4.66, 4.90, 3.20, 3.11 and 3.01, respectively, and the heat transfer stability of ISCMCADs with HETN of 18 is poor. As can be seen from Fig. 15 (b), the higher the HETN, the more the ice melted in the device and the higher the IMR. With the increase of HETN, the heat exchange area increases and the heat transfer process is enhanced, resulting in the increase of the IMR. During the 96 h heat exchange period, the IMR of the ISCMCAD with 18, 15, 12, 9 and 6 HETNs are 85.02%, 79.255%, 75.49%, 71.71% and 69.17%, respectively. Only ISCMCAD with 18 tubes have an IMR greater than 83.33% to meet the ice storage capacity utilization requirement. The larger the HETN, the higher the effect on the IMR. This can be explained that the larger the HETN, the larger the heat transfer area and thus the higher the heat flux. However, the higher the HETN will result in poorer cooling stability of the ISCMCAD during the 96 h cooling period. Combining the performance indices of ISCMCAD with different HETN, it can be concluded that during the 96 h heat transfer period, the ISCMCAD with 18 tubes has poor heat transfer stability but the highest IMR and the lowest AOT can meet the requirements of ice storage utilization. In summary, a model of ISCMCAD with 18 tubes is finally selected for the later study.

3.3.2 Effect of the IAT

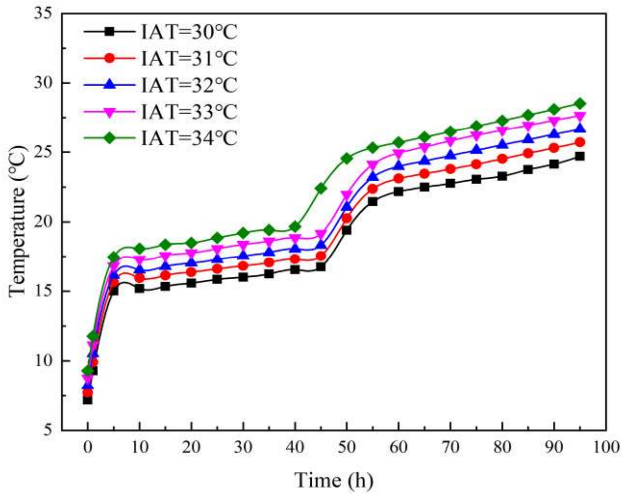

(a) OAT change curve

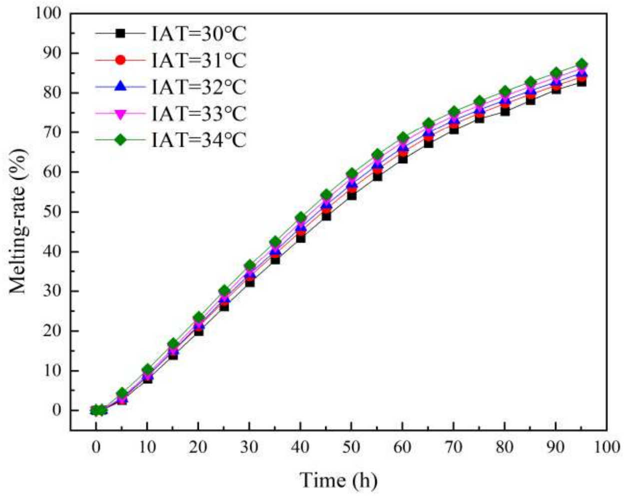

(b) IMR curve

Fig. 16. Heat transfer performance curve of ISCMCAD with different IATs at an IAV of 10 m/s and a HETN of 18

Fig. 16 plots the profile of different IAT on the OAT and IMR at an IAV of 10 m/s and HETN of 18. As can be seen from Fig. 16 (a) that the OAT increases with the increase of the IAT, and the heat transfer process can be divided into four stages. In the first stage, only sensible heat transfer occurs between the air and ice, the heat exchange time is short and the temperature rises greatly. In the second stage, the latent heat transfer dominates, and the heat exchange time decreases with the increase of IAT. In the third stage, the latent heat exchange gradually decreases, while the sensible heat exchange gradually increases. In the fourth stage, only sensible heat transfer occurs between the air and water, and the OAT rises slowly. It can be deduced that the increase in IAT reduces the latent heat exchange time. When the IAT is 30, 31, 32, 33 and 34℃, the OAT at 96 h is 24.70, 25.70, 25.96, 27.65 and 28.52℃, respectively, the cooling temperature difference (CTD) is between 5 and 6℃. As shown in Fig.16 (b), the larger the IAT, the larger the IMR. After 96 h of heat exchange, the IMR of the ISCMCAD was 82.72%, 84.03%, 85.02%, 86.17% and 87.30%, respectively. It can be known that when the IAT is higher than 31°C, the IMR is greater than 83.33%. In general, the utilization rate of the ice stored in the ISCMCAD is high during the whole heat exchange process.

3.3.3 Effect of the IAV

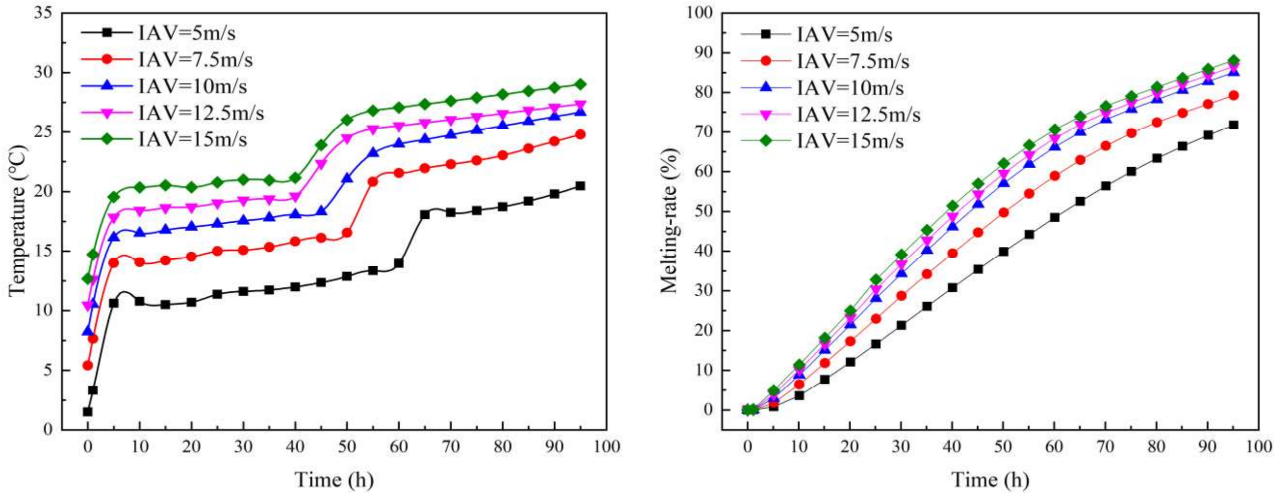

(a) OAT change curve **(b) IMR curve**

Fig. 17. Heat transfer performance curve of ISCMCAD with different IAVs at IAT of 32℃ and HETN of 18.

Fig. 17 shows the relationship between the OAT and the IMR of the ISCMCAD at different inlet air velocities with IAT of 32℃ and HETN of 18. From Fig. 17 (a), it can be observed that the influence of different IAV on the cooling effect of the ISCMCAD is larger. The OAT of the ISCMCAD increases with the increase of the IAV, indicating that the larger the IAV, the worse the cooling effect of the ISCMCAD. Because with the increase of IAV, the heat transfer time per unit mass of air decreases, while the air flow per unit time increases. The latent heat exchange time between the air and ice is inversely proportional to the IAV, and the sensible heat exchange time between the air and water is directly proportional to the IAV. After 96 h of heat exchange the IAV of 5 m/s, 7.5 m/s, 10 m/s, 12.5 m/s, 15 m/s correspond to the OAT of 20.46, 24.77, 26.67, 27.36, 29.02℃ respectively, and the CTD after 96 h is between 3 and 12℃. From Fig. 17 (b), it can be seen that the larger the IAV, the higher the utilization rate of the ice storage in the device. After 96 h heat exchange the IAV increases from 5 m/s to 15 m/s and the IMR increases from 71.71% to 88.07% which is increased by 16.36%. The reason could be the higher the IAV, the higher the flow rate through the device, this could result in a higher heat flux through the device according to the conservation of energy.

4. Discussion

4.1 Air supply method

As shown in Table 4, the supply air temperature required for MRCs with different ISRTs can be calculated referring to the air supply temperature prediction method given in Ref. [53]. The ADV is the total air volume required for 96 hours, which can be calculated when the cold storage capacity is 414600 kJ and the IMR is 83.33%. Then the IAV can be calculated according to the ADV and the diameter of the air inlet pipe. Additionally, the number of people that the ISCMCAD satisfied for MRCs with different ISRTs under different ADV can be obtained, considering that the per capita air volume is 0.3 m^3/min in the MRC. From Table 4, it can be concluded that the ISCMCAD needs to meet the air supply requirements for different ISRT in order to be suitable for MRCs with different ISRT.

Table 4 Calculation of air supply parameters for different ISRT

ISRT（℃）	T_V（℃）	CTD（℃）	ADV（m^3）	IAV（m/s）	Number of people
30	23.28	6.72	39667.51	14.61	23
31	21.83	9.17	29069.32	10.71	17
32	20.38	11.62	22940.25	8.45	13
33	18.93	14.07	18945.68	6.98	11
34	17.48	16.52	16135.94	5.94	9

When the ventilation parameters of the air inlet remain unchanged, the ventilation temperature entering the MRC from the air outlet of the ISCMCAD is uneven, resulting in a situation where the ambient temperature is low first and then high. From the above results, when the IAV is 7 m/s, the ISCMCAD can cool down the MCA from 31℃ to 21.5℃ within 96 hours, meaning that the ISCMCAD can satisfy 11 people at least within 96 h for the MRC with an ISRT of 31℃. However, when the IAT is 32℃ and the IAV is 10m/s, the ISCMCAD can reduce the MCA to within 20℃ in the first 50 hours, which can meet the air supply requirements of MRC, after 50 hours, the OAT of the ISCMCAD is higher than 20℃ and cannot meet the air supply requirements of MRC. Thus, a reasonable distribution of the ice storage capacity during the refuge period is the key to improve the utilization rate and extending the effective temperature control time of the MRC. The air supply characteristics of the building's air conditioning system are used to design a set of air supply methods for the ISCMCAD to meet the cooling requirements of the MRC.

As shown in Fig. 18 (a), the low temperature air produced by the ISCMCAD is mixed with the high temperature air from the MCA before entering into the MRC. In Fig. 18 (b), the corresponding mixed air volume can be obtained according to the enthalpy-humidity diagram and the conservation of energy, taking the MCA temperature of 32℃ and relative humidity of 55% as an example, it is represented as point *B* on the enthalpy-humidity diagram. Because the AOT within the first 50 hours of the ice storage device is 16℃, the OAT of the ISCMCAD is set to 16℃ and the relative humidity is 25%, which is represented by point *A* on the enthalpy-humidity chart. The supply air temperature of

MRC is set to 20°C. Connecting points, A and B on the enthalpy-humidity chart, the line AB intersects with the 20°C isotherm to obtain the supply air state point C. The enthalpy values of points A, B and C can be derived from the enthalpy-humidity diagram as h_A, h_B and h_C, respectively.

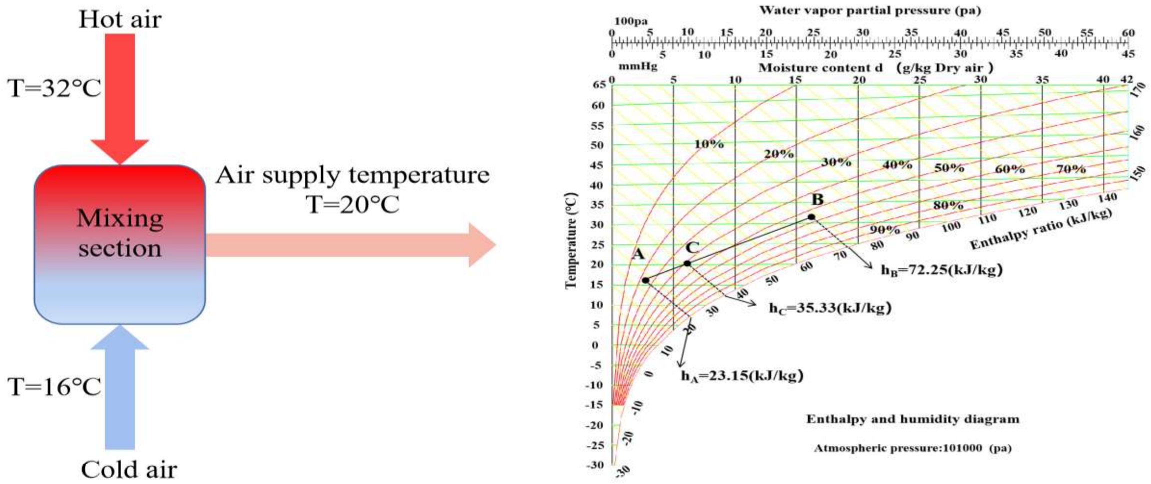

(a) Mixing Schematic **(b) Mixing principle**

Fig .18. Mixing air supply method.

The air volume at state point A and B can be calculated as follows:

$$q_1 \times h_A + q_2 \times h_B = M_a \times h_C \tag{28}$$

Where, q_1 is the air volume at state point A (kg/h), q_2 is the air volume at state point B (kg/h), and M_a is the air volume at state point C (kg/h). Here, M_a is 370.1 kg/h, h_A is 23.12 kJ/kg, h_B is 72.25 kJ/kg, h_C is 35.33 kJ/kg, q_1+q_2 = M_a. Among them q_1 is 278.12 kg/h and q_2 is 91.98kg/h.

According to the above mixed air supply method, the ISCMCAD can meet the air supply requirements of the MRC with an ISRT of 32°C. The numerical results show that the AOT of the ISCMCAD in 96 h with IAV of 10 m/s and IATs of 30, 31, 32, 33 and 34°C are 18.38, 19.27, 20.05, 20.92 and 21.88°C, respectively. According to Table 4, it can be concluded that for the MRC when the t ISRT is lower than 32°C, the cold source can be reasonably distributed through the mixed air supply method, so that the ISCMCAD can meet the cooling requirements within 96h. In engineering applications, the ratio of mixed air volume can be adjusted according to the actual MCA temperature, the actual cooling temperature of the ISCMCAD and the required supply air temperature to meet the requirements of temperature control of the MRC.

4.2 Performance comparison

Table 5 compares the configuration and performance of the ISCMCAD with the forced-circulation ice thermal storage device proposed in Ref. [50]. It can be found that compared with the forced-circulation ice thermal storage device, the ISCMCAD has new improvements in the structure of the tank and the heat exchange channels as well as the power mode, which not only improves the economy of the device, but also increases the number of users per unit volume of ice storage capacity. More importantly, through the mixed air supply way, the effective working time of the equipment in the evacuation environment can be extended to 96 hours, improving the thermal comfort of the evacuation environment.

Table 5 Comparison among the ice storage air conditioning systems

Ice storage air conditioner type	Ice storage volume	Power mode	Air conditioning structure	Applicable number of people	Temperature control effect	Effective cooling time
Forced-circulation ice thermal storage device [50]	5.5 m^3	Electric storage explosion-proof fan	Single rectangular tube	50	The temperature in the refuge chamber is below 35℃	64.57 h
ISACS	1 m^3	MCA	Multi-channel circular tube bundle	15	The temperature in the refuge chamber is below 30℃	96 h

5. Conclusions

In the current work, an ISCMCAD has been developed for high-temperature MRCs, and an experimental platform is newly built to test the thermal performance of the ISCMCAD. A full-size numerical model of the ISCMCAD has been established and validated against the experimental data. The effects of the HETN, IAV and IAT on the thermal performance are numerically investigated in a systematic manner. In order to rationalize the use of the cooling capacity and to explore the application of the ISCMCAD for MRCs, a mixing air supply method is proposed. The main conclusions are summarized below:

(1) When the ISCMCAD is exposed to the environment with an ambient temperature of 20 ~ 30℃, the water inside the tank will be completely frozen into ice with temperature below -15℃ after 60 h.

(2) When the HETN is 18, the best heat transfer performance of the ISCMCAD is achieved, the

MCA with an IAV of 10 m/s will be cooled to within 24.5℃ from 32℃ after 96 h, while the AOT is 20.53℃ and the IMR is 85.02%.

(3) For the case of IAV of 10 m/s, when the IAT increases from 30℃ to 34℃, it is observed that the IMR is increased by 4.59% and the AOT is increased by 3.5℃ after 96 h.

(4) For the case of IAT of 32℃, when the IAV increases from 5 m/s to 15 m/s, the IMR is increased by 16.36% and the AOT is increased by 10.26℃ after 96 h heat exchange.

(5) It is found that the heat transfer coefficient of the ISCMCAD is between 24.26-36.28 $W/m^2 \cdot K$, while the Nusselt number on the air side is 42.1.

(6) A mixed air supply method was proposed to allocate the cooling capacity of ISCMCAD reasonably. For MRC with ISRT of 32℃, the ISCMCAD can only meet the cooling demand of 8 people for 96 hours when air supplied directly, while it can meet the demand of 15 people when air supplied with mixed air.

Overall, the current study provides a practical basis for solving the problem of temperature control in high-temperature refuge chambers by using the combined temperature control technology of compressed air-device ice storage-surrounding rock cold storage. Future work will focus on the optimization of the heat transfer performance of the ice storage cooling device and the potential application of the ice storage cooling device for practical MRCs.

Declaration of competing interest

The authors declare that they have no known competing financial interests or personal relationships that could have appeared to influence the work reported in this paper.

Acknowledgments

The authors would like to thank the financial support from the National Natural Science Foundation of China (NO. 52168013 and NO.51908080), the Natural Science Foundation of Guizhou Province (No. ZK [2022]151 and No. [2020]2004) and the State Key Laboratory of Gas Disaster Detecting, Preventing and Emergency Controlling Open fund Project (No.2021SKLKF10).

References

[1] Z. Fareed, U.K. Pata, Renewable, non-renewable energy consumption and income in top ten renewable energy-consuming countries: advanced fourier based panel data approaches, Renew.

Energy 194 (2022) 805-821, https://doi.org/10.1016/j.renene.2022.05.156.
[2] L. Zhao, Z. Liu, L. Cheng, How will china's coal industry develop in the future? A quantitative analysis with policy implications, Energy 235 (2021) 121406, https://doi.org/https://doi.org/10.1016/j.energy.2021.121406.
[3] S. Rayegan, S. Motaghian, G. Heidarinejad, H. Pasdarshahri, P. Ahmadi, M.A. Rosen, Dynamic simulation and multi-objective optimization of a solar-assisted desiccant cooling system integrated with ground source renewable energy, Appl. Therm. Eng. 173 (2020), https://doi.org/10.1016/j.applthermaleng.2020.115210.
[4] C. Chang, X. Nie, X. Li, P. Tao, B. Fu, Z. Wang, J. Xu, Q. Ye, J. Zhang, C. Song, W. Shang, T. Deng, Bioinspired roll-to-roll solar-thermal energy harvesting within form-stable flexible composite phase change materials, J. Mater. Chem. A 8 (40) (2020) 20970-20978, https://doi.org/10.1039/D0TA07289C.
[5] T. Yang, W.P. King, N. Miljkovic, Phase change material-based thermal energy storage, Cell Rep. Phys. Sci. 2 (8) (2021) 100540, https://doi.org/https://doi.org/10.1016/j.xcrp.2021.100540.
[6] H. Mahon, D. O'Connor, D. Friedrich, B. Hughes, A review of thermal energy storage technologies for seasonal loops, Energy 239 (2022) 122207, https://doi.org/https://doi.org/10.1016/j.energy.2021.122207.
[7] W. Zhu, B. Huang, J. Zhao, X. Chen, C. Sun, Impacts on the embodied carbon emissions in china’s building sector and its related energy-intensive industries from energy-saving technologies perspective: a dynamic cge analysis, Energy Build. 287 (2023) 112926, https://doi.org/https://doi.org/10.1016/j.enbuild.2023.112926.
[8] A.T. Muzhanje, M.A. Hassan, H. Hassan, Phase change material based thermal energy storage applications for air conditioning: review, Appl. Therm. Eng. 214 (2022), https://doi.org/10.1016/j.applthermaleng.2022.118832.
[9] C. Lausselet, K.M. Lund, H. Brattebo, Lca and scenario analysis of a norwegian net-zero ghg emission neighbourhood: the importance of mobility and surplus energy from pv technologies, Build. Environ. 189 (2021), https://doi.org/10.1016/j.buildenv.2020.107528.
[10] M. Conci, T. Konstantinou, A. van den Dobbelsteen, J. Schneider, Trade-off between the economic and environmental impact of different decarbonisation strategies for residential buildings, Build. Environ. 155 (2019) 137-144, https://doi.org/10.1016/j.buildenv.2019.03.051.
[11] M. Schuller, Q. Shao, T. Lalk, Experimental investigation of the specific heat of a nitrate-alumina

nanofluid for solar thermal energy storage systems, Int. J. Therm. Sci. 91 (2015) 142-145, https://doi.org/10.1016/j.ijthermalsci.2015.01.012.

[12]M. Imran Khan, F. Asfand, S.G. Al-Ghamdi, Progress in research and development of phase change materials for thermal energy storage in concentrated solar power, Appl. Therm. Eng. 219 (2023) 119546, https://doi.org/https://doi.org/10.1016/j.applthermaleng.2022.119546.

[13]M. Fan, H.X. Suo, H. Yang, X.M. Zhang, X.F. Li, L.H. Guo, X.F. Kong, Experimental study on thermophysical parameters of a solar assisted cascaded latent heat thermal energy storage (clhtes) system, Energy 256 (2022), https://doi.org/10.1016/j.energy.2022.124639.

[14]Y. Liu, Z. Tian, C. Song, Y. Chen, Y. Li, J. Liu, Thermal performance and optimization of a casing pipe solar energy storage floor with phase change material, Energy Build. 247 (2021) 111167, https://doi.org/https://doi.org/10.1016/j.enbuild.2021.111167.

[15]W.Q. Li, T.Y. Zhang, B.B. Li, Z.R. Xue, H. Wang, D. Zhang, Enhanced energy management performances of passive cooling, heat storage and thermoelectric generator by using phase change material saturated in metal foam, Int. J. Therm. Sci. 184 (2023) 107869, https://doi.org/https://doi.org/10.1016/j.ijthermalsci.2022.107869.

[16]X. Luo, J.H. Wang, M. Dooner, J. Clarke, Overview of current development in electrical energy storage technologies and the application potential in power system operation, Appl. Energy 137 (2015) 511-536, https://doi.org/10.1016/j.apenergy.2014.09.081.

[17]Y. Ge, J.T. Han, X.X. Zhu, J.Y. Li, W.C. Zhu, J.W. Yang, W.X. Liang, Power/thermal-to-hydrogen energy storage applied to natural-gas distributed energy system in different climate regions of china, Energy Conv. Manag. 283 (2023), https://doi.org/10.1016/j.enconman.2023.116924.

[18]A. Aljehani, L.C. Nitsche, S. Al-Hallaj, Numerical modeling of transient heat transfer in a phase change composite thermal energy storage (pcc-tes) system for air conditioning applications, Appl. Therm. Eng. 164 (2020), https://doi.org/10.1016/j.applthermaleng.2019.114522.

[19]B. Nghana, F. Tariku, Phase change material's (pcm) impacts on the energy performance and thermal comfort of buildings in a mild climate, Build. Environ. 99 (2016) 221-238, https://doi.org/10.1016/j.buildenv.2016.01.023.

[20]A.K. Singh, P. Rathore, R.K. Sharma, N.K. Gupta, R. Kumar, Experimental evaluation of composite concrete incorporated with thermal energy storage material for improved thermal behavior of buildings, Energy 263 (2023), https://doi.org/10.1016/j.energy.2022.125701.

[21]S.W. Sharshir, A. Joseph, M. Elsharkawy, M.A. Hamada, A.W. Kandeal, M.R. Elkadeem, A.

Kumar Thakur, Y. Ma, M. Eid Moustapha, M. Rashad, M. Arıcı, Thermal energy storage using phase change materials in building applications: a review of the recent development, Energy Build. 285 (2023) 112908, https://doi.org/https://doi.org/10.1016/j.enbuild.2023.112908.
[22]X. Gao, Y. Yuan, H. Wu, X. Cao, X. Zhao, Coupled cooling method and application of latent heat thermal energy storage combined with pre-cooling of envelope: optimization of pre-cooling with intermittent mode, Sust. Cities Soc. 38 (2018) 370-381, https://doi.org/https://doi.org/10.1016/j.scs.2018.01.014.
[23]X. Gao, Z. Zhang, Y. Yuan, X. Cao, C. Zeng, D. Yan, Coupled cooling method for multiple latent heat thermal storage devices combined with pre-cooling of envelope: model development and operation optimization, Energy 159 (2018) 508-524, https://doi.org/https://doi.org/10.1016/j.energy.2018.06.151.
[24]X. Gao, Y. Yuan, X. Cao, H. Wu, X. Zhao, D. Yan, Coupled cooling method and application of latent heat thermal energy storage combined with pre-cooling of envelope: temperature control using phase-change chair, Sust. Cities Soc. 42 (2018) 38-51, https://doi.org/https://doi.org/10.1016/j.scs.2018.06.032.
[25]M.S. Yousef, H. Hassan, Energetic and exergetic performance assessment of the inclusion of phase change materials (pcm) in a solar distillation system, Energy Conv. Manag. 179 (2019) 349-361, https://doi.org/10.1016/j.enconman.2018.10.078.
[26]J.W. Guo, B. Zou, Y. Wang, Y.Q. Jiang, Space heating performance of novel ventilated mortar blocks integrated with phase change material for floor heating, Build. Environ. 185 (2020), https://doi.org/10.1016/j.buildenv.2020.107175.
[27]H. Selvnes, Y. Allouche, R.I. Manescu, A. Hafner, Review on cold thermal energy storage applied to refrigeration systems using phase change materials, Therm. Sci. Eng. Prog. 22 (2021), https://doi.org/10.1016/j.tsep.2020.100807.
[28]R.Y. Cheng, J.Q. Yu, M. Zhang, C.Y. Feng, W.H. Zhang, Short-term hybrid forecasting model of ice storage air-conditioning based on improved svr, J. Build. Eng. 50 (2022), https://doi.org/10.1016/j.jobe.2022.104194.
[29]M. De Falco, M. Capocelli, A. Giannattasio, Performance analysis of an innovative pcm-based device for cold storage in the civil air conditioning, Energy Build. 122 (2016) 1-10, https://doi.org/10.1016/j.enbuild.2016.04.016.
[30]H. Kitagawa, T. Asawa, T. Kubota, A.R. Trihamdani, Numerical simulation of radiant floor

cooling systems using pcm for naturally ventilated buildings in a hot and humid climate, Build. Environ. 226 (2022), https://doi.org/10.1016/j.buildenv.2022.109762.

[31] S. Sanaye, A. Shirazi, Thermo-economic optimization of an ice thermal energy storage system for air-conditioning applications, Energy Build. 60 (2013) 100-109, https://doi.org/10.1016/j.enbuild.2012.12.040.

[32] D. Erdemir, N. Altuntop, Y.A. Cengel, Experimental investigation on the effect of ice storage system on electricity consumption cost for a hypermarket, Energy Build. 251 (2021), https://doi.org/10.1016/j.enbuild.2021.111368.

[33] X.S. Fang, K.L. Huang, G.H. Feng, W.H. Cai, J.S. Song, H.X. Li, G. Li, Experimental and numerical research on the performance of a seasonal ice storage device in summer residential rooms of northeast china, Sust. Cities Soc. 75 (2021), https://doi.org/10.1016/j.scs.2021.103334.

[34] X. Song, L.C. Liu, T. Zhu, S. Chen, Z.J. Cao, Study of economic feasibility of a compound cool thermal storage system combining chilled water storage and ice storage, Appl. Therm. Eng. 133 (2018) 613-621, https://doi.org/10.1016/j.applthermaleng.2018.01.063.

[35] S.M. Miri, M. Farzaneh-Gord, A. Kianifar, Evaluating the dynamic behaviour of wind-powered compression refrigeration cycle integrated with an ice storage tank for air conditioning application, Energy Conv. Manag. 269 (2022), https://doi.org/10.1016/j.enconman.2022.116093.

[36] M.H. Randar, A. Emamzadeh, A. Ataei, A comparative study on pcm and ice thermal energy storage tank for air-conditioning systems in office buildings, Appl. Therm. Eng. 96 (2016) 391-399, https://doi.org/10.1016/j.applthermaleng.2015.11.107.

[37] Y.F. Xu, M. Li, X. Luo, X. Ma, Y.F. Wang, G.L. Li, R. Hassanien, Experimental investigation of solar photovoltaic operated ice thermal storage air-conditioning system, Int. J. Refrig. 86 (2018) 258-272, https://doi.org/10.1016/j.ijrefrig.2017.11.035.

[38] A.E. Halim, J.F. Brune, Do refuge chambers represent a good strategy to manage emergencies in underground coal mines? Mining, Metallurgy & Exploration 36 (6) (2019) 1191-1199, https://doi.org/10.1007/s42461-019-0100-8.

[39] K.E. Karadeniz, S. Nowak, D. Guner, T. Sherizadeh, Evaluation on underground refuge alternatives and explosion survivability: a review, Mining Metall. Explor. 39 (6) (2022) 2311-2331, https://doi.org/10.1007/s42461-022-00682-1.

[40] Y. Li, Y.P. Yuan, C.F. Li, X. Han, X.S. Zhang, Human responses to high air temperature, relative humidity and carbon dioxide concentration in underground refuge chamber, Build. Environ. 131

(2018) 53-62, https://doi.org/10.1016/j.buildenv.2017.12.038.

[41] H. Shao, S. Jiang, W. Tao, Z. Wu, W. Zhang, K. Wang, Theoretical and numerical simulation of critical gas supply of refuge chamber, Int. J. Min. Sci. Technol. 26 (3) (2016) 389-393, https://doi.org/https://doi.org/10.1016/j.ijmst.2016.02.004.

[42] C.D. Ashley, R.M. Lopez, X.P. Garzon-Villalba, T.E. Bernard, Thermal exposure limit in a simulated refuge alternative, Mining Metall. Explor. 37 (1) (2020) 179-186, https://doi.org/10.1007/s42461-019-00134-3.

[43] Z.J. Zhang, H.W. Wu, K.Q. Wang, R. Day, Y.P. Yuan, Air quality control in mine refuge chamber with ventilation through pressure air pipeline, Process Saf. Environ. Protect. 135 (2020) 46-58, https://doi.org/10.1016/j.psep.2019.12.014.

[44] Z.J. Zhang, H.W. Wu, K.Q. Wang, R. Day, Y.P. Yuan, Thermal performance of a mine refuge chamber with human body heat sources under ventilation, Appl. Therm. Eng. 162 (2019), https://doi.org/10.1016/j.applthermaleng.2019.114243.

[45] X.K. Gao, Z.J. Zhang, Y.M. Xiao, Modelling and thermo-hygrometric performance study of an underground chamber with a long vertical earth-air heat exchanger system, Appl. Therm. Eng. 180 (2020), https://doi.org/10.1016/j.applthermaleng.2020.115773.

[46] Y.P. Yuan, X.K. Gao, H.W. Wu, Z.J. Zhang, X.L. Cao, L.L. Sun, N.Y. Yu, Coupled cooling method and application of latent heat thermal energy storage combined with pre-cooling of envelope: method and model development, Energy 119 (2017) 817-833, https://doi.org/10.1016/j.energy.2016.11.058.

[47] J.L. Yang, L.W. Yang, J. Wei, Y.Z. Ma, Z.T. Zhang, Study on open-cycle carbon dioxide refrigerator for movable mine refuge chamber, Appl. Therm. Eng. 52 (2) (2013) 304-312, https://doi.org/10.1016/j.applthermaleng.2012.12.014.

[48] L.C. Yan, D. Yantek, M. Reyes, B. Whisner, J. Bickson, J. Srednicki, N. Damiano, E. Bauer, Cryogenic air supply for cooling built-in-place refuge alternatives in hot mine, Mining Metall. Explor. 37 (3) (2020) 861-871, https://doi.org/10.1007/s42461-020-00194-w.

[49] Y. Du, W.M. Gai, L.Z. Jin, W. Sheng, Thermal comfort model analysis and optimization performance evaluation of a multifunctional ice storage air conditioning system in a confined mine refuge chamber, Energy 141 (2017) 964-974, https://doi.org/10.1016/j.energy.2017.09.123.

[50] W. Shu, L.Z. Jin, Z.L. Han, Y.G. Li, S.N. Ou, G. Na, Z.L. Huang, Discharging performance of a forced-circulation ice thermal storage system for a permanent refuge chamber in an underground mine,

Appl. Therm. Eng. 110 (2017) 703-709, https://doi.org/10.1016/j.applthermaleng.2016.08.192.

[51]X. Xu, S.J. You, X.J. Zheng, H. Zhang, S. Liu, Cooling performance of encapsulated ice plates used for the underground refuge chamber, Appl. Therm. Eng. 112 (2017) 259-272, https://doi.org/10.1016/j.applthermaleng.2016.10.072.

[52]Y.X. Jia, Y.S. Liu, S.F. Sun, H.Y. Li, L.L. Jiao, Refrigerating characteristics of ice storage capsule for temperature control of coal mine refuge chamber, Appl. Therm. Eng. 75 (2015) 756-762, https://doi.org/10.1016/j.applthermaleng.2014.10.036.

[53]Z.J. Zhang, W.S. Guo, X.K. Gao, H.W. Wu, R.Y. Mao, Investigation on temperature control based on cooled mine compressed air for mine refuge chamber with high-temperature surrounding rock, Int. J. Therm. Sci. 187 (2023), https://doi.org/10.1016/j.ijthermalsci.2023.108201.

[54]F. Afsharpanah, K. Pakzad, S.S. Mousavi Ajarostaghi, S. Poncet, K. Sedighi, Accelerating the charging process in a shell and dual coil ice storage unit equipped with connecting plates, Int. J. Energy Res. 46 (6) (2022) 7460-7478, https://doi.org/10.1002/er.7654.

[55]F. Afsharpanah, G. Cheraghian, F. Akbarzadeh Hamedani, E. Shokri, S.S. Mousavi Ajarostaghi, Utilization of carbon-based nanomaterials and plate-fin networks in a cold pcm container with application in air conditioning of buildings, Nanomaterials 12 (11) (2022) 1927, https://doi.org/10.3390/nano12111927.

[56]F. Afsharpanah, M. Izadi, F.A. Hamedani, S.S. Mousavi Ajarostaghi, W. Yaïci, Solidification of nano-enhanced pcm-porous composites in a cylindrical cold thermal energy storage enclosure, Case Stud. Therm. Eng. 39 (2022) 102421, https://doi.org/10.1016/j.csite.2022.102421.

[57]F. Afsharpanah, S.S. Mousavi Ajarostaghi, M. Arıcı, Parametric study of phase change time reduction in a shell-and-tube ice storage system with anchor-type fin design, Int. Commun. Heat Mass Transf. 137 (2022) 106281, https://doi.org/10.1016/j.icheatmasstransfer.2022.106281.

[58]D. Macphee, I. Dincer, A. Beyene, Numerical simulation and exergetic performance assessment of charging process in encapsulated ice thermal energy storage system, Energy 41 (1) (2012) 491-498, https://doi.org/10.1016/j.energy.2012.02.042.

[59]Z.J. Zhang, T. Jin, H.W. Wu, R. Day, X.K. Gao, K.Q. Wang, R.Y. Mao, Experimental investigation on environmental control of a 50-person mine refuge chamber, Build. Environ. 210 (2022), https://doi.org/10.1016/j.buildenv.2021.108667.

[60]R. Kwidzinski, Condensation heat and mass transfer in steam–water injectors, Int. J. Heat Mass Transf. 164 (2021) 120582, https://doi.org/https://doi.org/10.1016/j.ijheatmasstransfer.2020.120582.

[61]J. Wu, S. Liu, M. Wang, Process calculation method and optimization of the spiral-wound heat exchanger with bilateral phase change, Appl. Therm. Eng. 134 (2018) 360-368, https://doi.org/https://doi.org/10.1016/j.applthermaleng.2018.01.128.

[62]Z. Zhang, H. Wu, K. Wang, R. Day, Y. Yuan, Air quality control in mine refuge chamber with ventilation through pressure air pipeline, Process Saf. Environ. Protect. 135 (2020) 46-58, https://doi.org/https://doi.org/10.1016/j.psep.2019.12.014.

[63]B. Du, Y. He, Y. Qiu, Q. Liang, Y. Zhou, Investigation on heat transfer characteristics of molten salt in a shell-and-tube heat exchanger, Int. Commun. Heat Mass Transf. 96 (2018) 61-68, https://doi.org/https://doi.org/10.1016/j.icheatmasstransfer.2018.05.020.

[64]J.Y. Chen, C.C. Chen, Uncertainty analysis in humidity measurements by the psychrometer method, Sensors 17 (2) (2017), https://doi.org/10.3390/s17020368.

[65]A. Kumar, S.K. Saha, Performance study of a novel funnel shaped shell and tube latent heat thermal energy storage system, Renew. Energy 165 (2021) 731-747, https://doi.org/10.1016/j.renene.2020.11.023.

[66]D. Yang, R. Shi, H.B. Wei, J.H. Du, J. Wang, Investigation of the performance of a cylindrical pcm-to-air heat exchanger (pahe) for free ventilation cooling in fluctuating ambient environments, Sust. Cities Soc. 51 (2019), https://doi.org/10.1016/j.scs.2019.101764.

[67]Z.C. Liu, Z.H. Quan, Y.H. Zhao, H.R. Jing, L.C. Wang, X. Liu, Numerical research on the solidification heat transfer characteristics of ice thermal storage device based on a compact multichannel flat tube-closed rectangular fin heat exchanger, Energy 239 (2022), https://doi.org/10.1016/j.energy.2021.122381.

[68]D. Li, C.X. Yang, H. Yang, Experimental and numerical study of a tube-fin cool storage heat exchanger, Appl. Therm. Eng. 149 (2019) 712-722, https://doi.org/10.1016/j.applthermaleng.2018.12.024.

[69] M. Izadi, S.F. Taghavi, S.H. Neshat Safavi, F. Afsharpanah, W. Yaïci, Thermal management of shelter building walls by pcm macro-encapsulation in commercial hollow bricks, Case Stud. Therm. Eng. 47 (2023) 103081, https://doi.org/https://doi.org/10.1016/j.csite.2023.103081.